NASA CONTRACTOR REPORT

NASA CR-74

NASA CR-740

ERROR ANALYSIS OF CELESTIAL-INERTIAL NAVIGATION FOR LOW-THRUST INTERPLANETARY VEHICLES

by Alan L. Friedlander

Prepared by
IIT RESEARCH INSTITUTE
Chicago, Ill.
for Ames Research Center

NATIONAL AERONAUTICS AND SPACE ADMINISTRATION • WASHINGTON, D. C. • APRIL 1967

NASA CR-740

ERROR ANALYSIS OF CELESTIAL-INERTIAL NAVIGATION FOR LOW-THRUST INTERPLANETARY VEHICLES

By Alan L. Friedlander

Prepared under Contract No. NAS 2-3348 by
IIT RESEARCH INSTITUTE
Chicago, Ill.

for Ames Research Center

NATIONAL AERONAUTICS AND SPACE ADMINISTRATION

For sale by the Clearinghouse for Federal Scientific and Technical Information
Springfield, Virginia 22151 – CFSTI price $3.00

FOREWARD

This report documents the work performed by the IIT Research Institute, Chicago, Illinois in fulfillment of the requirements of the National Aeronautics and Space Administration Contract No. NAS 2-3348. This contract was administered under the technical cognizance of Messrs. John S. White and Gerald L. Smith of the Ames Research Center, Moffett Field, California.

Studies presented in this report began in December, 1965 and were concluded in October, 1966. The work was preformed by the Guidance and Control Section under the direction of Alan L. Friedlander as Project Engineer. Principal contributors to the project were Messrs. A. Friedlander and R. Lang.

TABLE OF CONTENTS

ERROR ANALYSIS OF CELESTIAL-INERTIAL NAVIGATION FOR LOW-THRUST INTERPLANETARY VEHICLES

1. INTRODUCTION

The purpose of this research study has been to investigate the performance and requirements of celestial-inertial navigation applied to low-thrust (electric propulsion) space vehicles. By definition, navigation refers to the process of estimating the vehicle's state of motion given certain measurements of the input/output determinants of this motion. The navigational information is then used by the guidance and control subsystem to direct the vehicle to its desired target. Although the guidance problem is not explicitly considered in this study, it is understood that the accuracy and efficiency of guidance ultimately depends upon the accuracy of navigation.

The present investigation is an extension of previous work accomplished on the low-thrust navigation problem which was performed for Ames Research Center under Contract No. NAS 2-2401 (Ref. 1). This earlier study gives the mathematical formulation of the navigation concept and presents results of a numerical performance analysis of navigation during the midcourse, or heliocentric, phase of low-thrust interplanetary missions. The objectives of the present study are:

(1) To apply the navigation concept to the planetocentric phases of interplanetary missions, i.e., the escape and capture spiral phases.

(2) To evaluate the navigation performance for several complete interplanetary missions.

(3) To investigate the effect of incorrect assumptions in the a priori statistical data. That is, how do the true and estimated navigation errors compare when incorrect a priori covariance data are used in the state estimation procedure?

This report describes the navigation system in summary fashion, and also the principal features of the digital computer program developed during the course of this study to evaluate the navigation system performance. The remaining and major part of this report discusses the results obtained according to the study objectives stated above.

2. DESCRIPTION OF THE NAVIGATION SYSTEM

The navigation system assumed in this study utilizes both celestial and inertial source information for in-flight determination of vehicle motion. The celestial observations provide the means for significantly reducing the long term effects of the inertial gyro and accelerometer errors. Figure 1(a) illustrates the navigation system concept in functional block diagram form. A pair of gimballed star trackers (stellar monitor) integral with the inertial measurements unit serve to align and stabilize the space-fixed coordinate frame. Additional celestial sensors such as planet trackers or sextants measure appropriate space angles from which vehicle position may be found.

Of principal interest here is the navigation computer whose main function is to process the available information so as to obtain the best estimate of the vehicle state in the presence of random instrumentation errors. Figure 1(b) shows the computational structure of the state estimation procedure. The form of the estimator was orginally established by Kalman (Ref. 2) with the aid of linear statistical filter theory, and has since been applied extensively by others to the problem of spacecraft trajectory determination (Refs. 3,4). Commonly used names for this method are "dynamic filtering" and "sequential, minimum-variance estimation".

The vehicle state includes, in addition to the position and velocity coordinates, instrumentation errors having time-correlated statistical properties - hence, the estimation procedure allows in-flight calibration and correction of certain types of instrumentation errors. Of particular importance here is the estimation of accelerometer bias (or low-frequency random noise) - the accuracy of which may be significantly improved over Earth-based calibration methods. As indicated in Figure 1(b), celestial angle measurements are assumed to be made at discrete times whereas acceleration measurements are assumed continuous (or, effectively continuous in comparison to the celestial sampling rate). The filtering process is also discrete. At the celestial measurement time, the weighted difference between the measured and predicted space angle is the incremental correction applied to the previous estimate of the state. The new, and on-the-average improved, estimate serves as the updated initial condition used in the solution of the dynamical state equations over the next cycle.

2.1 Celestial Instrumentation Errors

Stellar Monitor

The function of the stellar monitor subsystem is to track selected stars of known position thereby providing the necessary information to measure and correct for inertial platform misalignment resulting from gyro drift. The attitude measurements are obtained from the gimbal angles of the two star trackers comprising the stellar monitor. Assuming a proportional plus integral correction procedure, it can be shown that the platform misalignment angles remaining after correction are, effectively, the angular errors of the stellar monitor. This is true for both constant and random input errors. For simplicity, we assume continuous operation of the stellar monitor and also neglect cross-coupling between axes. The error in each axis is assumed to be a zero-mean random variable described by a "band-limited" white noise process, i.e., an exponential autocorrelation function of the form

$$\phi_\eta(\tau) = \sigma_\eta^2 \, e^{-\frac{|\tau|}{\tau_\eta}} \tag{1}$$

where σ_η^2 and τ_η are, respectively, the variance and correlation time constant of the stellar monitor error. Generally, the correlation time is small as representive of relatively high-frequency noise. Stationary statistics are assumed for the stellar monitor error, as is the case for all other random instrumentation errors considered in this analysis.

Planet Sensor

The planet sensor subsystem provides direction angles to selected celestial bodies of the solar system (principally planets and moons), and, in the case of "near" bodies, also the subtended angle of the apparent disk from which range may be found directly. These planetary observations yield vehicle position information which serves mainly to compensate for the unbounded effect of the accelerometer errors. Without regard to the specific configuration of the planet sensors (e.g., theodolite, sextant or horizon scanner instrumentation types), the basic error of the sensor is assumed to be a zero-mean random variable whose variance is of the form

$$\sigma_\phi^2 = \sigma_n^2 + \frac{\sigma_R^2}{r^2 - R^2} \qquad (2)$$

where σ_n is the error attributed to the sensor optics and readout, and σ_R is the radius uncertainty of the planetary disk or horizon. Of course, when the vehicle is at a great distance from the planet the first term in (2) will predominate.

For the purpose of this analysis, it is assumed that the planet sensor is an integral part of the inertial measurement unit, i.e., the measured planet angles are referenced to the space-fixed axes of the inertial platform. In this case, the stellar monitor error contributes to the total measurement error as in the following equation

$$\sigma^2 = \sigma_\theta^2 + \sigma_\eta^2 \qquad (3)$$

where the errors in θ and η are assumed to be uncorrelated.

2.2 Inertial Instrumentation Errors

Gyro Drift

For the purpose of trajectory estimation, the gyro errors need not be considered inasmuch as the stellar monitor observation and correction process effectively eliminates gyro drift as a significant error source.

Accelerometer Error

The error model for the accelerometer assumes two independent random error sources, each of which is described by a stationary exponential auto-correlation function.

$$\phi_{ah}(\tau) = \sigma_{ah}^2 e^{-\frac{|\tau|}{\tau_{ah}}} \tag{4}$$

$$\phi_{a\ell}(\tau) = \sigma_{a\ell}^2 e^{-\frac{|\tau|}{\tau_{a\ell}}} \tag{5}$$

The first of these error components could be associated with a relatively high-frequency noise characteristic whose correlation time τ_{ah} is quite short-on the order of minutes. The second component represents low-frequency or bias type noise where $\tau_{a\ell}$ is a long correlation time - on the order of days. In particular, if $\tau_{a\ell} = \infty$, the low-frequency noise is a pure bias. Each component is assumed to have a zero-mean value. Further, each accelerometer in the 3-axis inertial system is assumed to have errors which are mutually independent.

To simplify the computation with little sacrifice in accuracy, the high-frequency accelerometer error is modeled as a "white noise" process having the auto-correlation function

$$\phi_{ah}(\tau) = 2\sigma_{ah}^2\tau_{ah}\delta(\tau) \tag{6}$$

where $\delta(\tau)$ is the Dirac delta (unit impulse) function.

3. DESCRIPTION OF THE COMPUTER PROGRAM

Actually, two separate computer programs were employed in the numerical analysis of navigation performance. The first program, developed during the course of the previous year's work (Ref. 1), was designed specifically for navigation during the heliocentric phase of an interplanetary mission. This program, written in FORTRAN II, was not directly applicable to a study of navigation during the planetocentric phases for the following reasons: (1) the heliocentric reference trajectories were of an optimal type and were computed concurrently with the navigation performance simulation. The variational calculus equations which defined the optimal thrust program were unnecessary for the planetocentric phase since the latter assumed a continuous, tangential thrust program (which is known to be near-optimal), (2) the heliocentric trajectories were computed in two-dimensions only under the assumed influence of a single, inverse-square gravitational field, and (3) the celestial observation policy during the planetocentric phase of flight differs from that during the heliocentric phase.

It was thought more expediant to develop a new computer program to handle the planetocentric navigation problem. Two basic subroutines of the former program are incorporated with slight modification. These are (1) the fourth-order Runge-Kutta numerical integration package, and (2) the optimal filter and covariance equations of the minimum variance estimation scheme.

The new program is written in FORTRAN IV for use on the IBM 7094 computer. Single precision arithmetic is used throughout with the exception of the variables of integration which are accumulated in double precision in order to minimize round-off error. Numerical integration may be carried out with either a fixed or automatically variable step size. The latter option is most suited to the planetocentric spiral trajectory which has a continuously and widely varying period of revolution.

The program does not include the provision for processing either real or simulated observational data. Rather, only the error statistics or covariance matrix of the navigation variables are computed. The linearized state transition and observation matrices needed in the covariance matrix computation are numerically evaluated about a fixed reference trajectory. This trajectory is computed simultaneously with the error covariance matrix.

Additional description and features of the planetocentric navigation computer program are outlined below:

1) Gravitational Model
    a) primary body including second harmonic oblateness terms (Earth or target planet)
    b) one secondary body (Moon), no oblateness, position determined from orbital elements.
2) Thrust Acceleration
    a) constant thrust or constant acceleration option
    b) tangentially directed thrust (along or opposite to velocity)

3) <u>Equation of Motion</u>

   a) Cowell's formulation - rectangular position and velocity components referenced to space-fixed axes of on-board inertial measurement unit, primary body is center of coordinate system.

   b) transformation provided between on-board reference axes and equatorial axes of primary body.

4) <u>Celestial Observation Policy</u>

   a) <u>Observables</u> (4 options)

      - direction of primary body (2 angles referenced to on-board axes)
      - direction and angular diameter of primary body
      - direction of primary and secondary bodies
      - direction of primary and secondary bodies, and angular diameter of primary body.

   b) <u>Observation Schedule</u> (2 options)

      - fixed time interval, specified by input
      - fixed number of observations per orbit with maximum time interval, specified by input

5) <u>Initialization</u>

   a) <u>Reference Trajectory</u> (2 options)

      - rectangular position and velocity in on-board inertial axis system
      - orbital elements referred to equator of primary body

   b) Covariance matrix in position-velocity space referred to on-board axes, non-diagonal initial covariance allowed but seldom used.

4. RESULTS AND DISCUSSION

Results of the low-thrust navigation study are presented in this section in the order of the study objectives stated in the introductory remarks. For the most part, the results are of numerical form and were obtained from the digital computer program described in the previous section. Certain analytical results which serve a better understanding of the navigation problem are also presented.

The first topic considered is that of navigation during the planetocentric maneuvers - principally, the Earth-escape spiral. Some interesting characteristics of the escape trajectory are discussed, however, there is no intent to fully cover this subject which has previously received much attention in the literature. The practical problems related to a numerical investigation of planetocentric navigation came to light early in this study. Mainly, this problem is one of extremely long running time of the computer program. The nature of the escape spiral (several hundred revolutions about Earth) requires a relatively large number of integration steps per orbit if one wishes to maintain even moderate accuracy. Another contributor to long running times is the frequency of celestial observations which should not be too low in order to compensate for the unbounded effect of accelerometer errors. It was estimated that 30-45 minutes of IBM 7094 time would be required to obtain the complete planetocentric escape solution beginning from a circular orbit of 1000 km altitude. This being only one solution, it is evident that any type of parametric analysis would be prohibitively costly. It was decided, therefore, to obtain navigation performance data only over two separated segments of the escape trajectory. The first segment covers about 36 hours (16 revolutions) in the low-altitude region. The second segment begins at a later time in flight (50,000 km near-circular orbit) and continues on to the Earth-escape conditions. This segment covers approximately 27 days and 7 revolutions. A parametric analysis of the navigation problem was made only for this latter trajectory segment.

The second topic of discussion is navigation performance for complete interplanetary missions. Four such missions are considered:

1) Mars Orbiter Mission - 205.4 day heliocentric transfer
2) Venus Orbiter Mission - 120 day heliocentric transfer
3) Mars Flyby Mission - 120 day heliocentric transfer
4) Jupiter Flyby Mission - 360 day heliocentric transfer

The orbiter missions terminate in a circular satellite orbit about the target planet - 10,000 km at Mars and 20,000 km at Venus. This relatively high-altitude terminal condition is necessitated again by the constraint of program running time. Each interplanetary mission is pieced together from the three essentially distinct phases; Earth-escape, heliocentric transfer, planet-capture (or flyby). The navigation conditions (estimation covariances) existing at the termination of one phase serve as the initial conditions for the succeeding phase. In view of the preliminary nature of this study, no attempt is made to optimize the entire mission either in terms of the vehicle configuration or propulsion system. Thus, for example, the same Earth-escape phase trajectory is assumed for each of the interplanetary missions. This should not detract from the navigation analysis since it can be established that the navigation performance is, within reasonable limits, a weak function of propulsion system parameters and operational modes.

The third topic of discussion concerns the question of how do the true and estimated navigation errors compare when incorrect a priori covariance data are used to initialize the state estimation procedure. Some answers to this question are presented in the case of Earth-escape navigation.

4.1 Navigation During Planetocentric Maneuvers

4.1.1 Trajectory Characteristics

A typical Earth-escape trajectory under low-thrust acceleration would be initiated from a near-circular satellite orbit at relatively low altitudes (200-1000 n. miles). The initial thrust acceleration for representative vehicle/propulsion systems would lie in the range 10^{-5} - 10^{-4} g's (Earth-surface gravity units). Assuming a tangentially directed thrust program, the vehicle will gradually increase its energy and altitude while remaining in a near-circular orbit. Eventually, during the last several revolutions about Earth, the vehicle will break away from the near-circular conditions and spiral out to a specified escape energy condition (parabolic or hyperbolic). For a thrust acceleration of 10^{-3} m/sec^2 (10^{-4}g), parabolic energy would be attained at about 600,000 km from Earth.

As the vehicle continues thrusting, it establishes a hyperbolic trajectory relative to Earth and moves along an asymptote that has a nearly constant direction in inertial space. The escape-spiral trajectory is designed so that the hyperbolic asymptote is pointed in a prescribed direction with reference to the ecliptic plane and the Earth-Sun line. In other words, the last spiral turn must be properly oriented. Since the vehicle makes several hundred revolutions about Earth in the process of escaping, it might be expected that the escape direction would be highly sensitive to errors. This expectation is amply verified by the results of a previous sensitivity analysis (Ref. 5). For example, a 0.1 percent error in either the initial orbital altitude or the initial mass, if left uncorrected, is sufficient to reverse the direction of escape. A minimum error of about 0.1 percent in the thrust magnitude acting over the entire trajectory will also result in a 180° misorientation. Because of the small control errors involved, the vehicle must have the capability of corrective-guidance programming. This, of course, implies the capability of state estimation or navigation.

Perturbations due to Earth oblateness and the lunar gravitational field result in some interesting effects on the escape spiral trajectory. Some of these perturbing effects are quite significant and must be taken into account in the actual planning of a space mission. Other effects are mainly of academic interest.

The equations shown in Table I describe the principal effect of both oblateness (2nd harmonic only) and thrust acceleration on the standard orbital elements. The region of applicability here is the near-circular spirals at the lower altitudes, i.e., semi-major axis approximately equal to radial distance and eccentricities in the range 10^{-4} to 10^{-2}. The equatorial plane is the reference plane for the orientation angles, i. and Ω.

Oblateness is seen to introduce harmonic oscillations in the orbital elements r, e, ω and i but, in general, no appreciable secular changes. The principal effect of oblateness on the mission trajectory is a regression of the line of nodes, Ω. This rotation of the orbital plane can be as large as 8° per day for a vehicle beginning from a 300 mile circular orbit, and the total rotation for typical thrust levels could be as large as 50°. Since the oblateness acceleration at the lower altitudes is usually an order of magnitude larger than the available thrust acceleration, the rotation of the plane cannot be counteracted by thrust. For those missions where the orientation of the plane is important, the predictable regression of the nodes must be taken into account by the choice of nominal initial orientation.

Under the thrust acceleration column of Table I one notes that the escape spiral can be made nonoscillatory (i.e., r, e and ω increase monotonically) by a suitable choice of initial conditions, namely, an initial eccentricity equal to twice the ratio of thrust to gravity acceleration and a true anomoly near 90°. While the nonoscillatory escape spiral offers no special advantages in terms of payload performance, it does offer a significant advantage in terms of reduced numerical integration times and simplified expressions for guidance purposes. Unfortunately, the inclusion of oblateness negates the effect of the nonoscillatory initial conditions.

Figure 2 illustrates the combined effect of oblateness and thrust over the first two revolutions of an Earth-escape spiral beginning in an orbit of 500 km altitude and 45° inclination with a thrust acceleration of 10^{-3} m/sec^2. These results are obtained by numerical integration. The rate of change of r is quite variable but is mostly of a positive sense. Eventually (at the higher altitudes) the oscillations in r and e become damped to negligible values and thereafter, these quantities increase monotonically. Figure 3 shows these quantities as a function of time beginning from a 50,000 km orbit and extending to the escape (parabolic) energy condition.

The action of the Moon as a perturbing influence on the escape spiral is illustrated by Figure 4. In this example, the orbital planes of the vehicle and Moon are nearly matched and the closest approach to the Moon is 28,000 km. This particular gravitational encounter adds about 400 m/sec to hyperbolic excess velocity and causes the outgoing asymptote to regress by 25°. Although the Moon offers a moderate amount of "free" energy addition, the usefulness of this flight mode would ultimately depend upon other mission considerations such as timing in relation to target constraints and also guidance accuracy. In general, if this energy addition is not called for, it should be relatively easy to avoid the perturbing influence of the Moon.

4.1.2 Navigation Performance at Low Altitudes

The performance of the celestial-inertial navigation system is first illustrated for the low-altitude segment of the Earth-escape spiral. The vehicle is assumed to begin the spiral from a near-circular orbit of 45° inclination and altitude of 1000 n. mile ($r = 8230$ km), and a thrust acceleration of 10^{-3} m/sec^2. Table II lists the nominal error parameter values which are assumed. Initial position and velocity uncertainties are 1 km and 1 m/sec in each component. All optical instrumentation errors are assumed 10 seconds of arc, and the horizon error is 3.2 km. Correlation time constants of the low and high frequency accelerometer errors are, respectively, ∞ (bias) and 30 minutes. The RMS magnitude of each accelerometer error component is assumed 10^{-5} m/sec^2 for the results to be given in this section. Later, a lower value of 10^{-6} m/sec^2 will be taken as nominal and so indicated. The celestial observables are the direction angles and subtended diameter of Earth taken at 15 minute intervals.

Figures 5(a) - (d) show the time histories of the RMS state estimation errors during the early part of the Earth-escape spiral. In the case of position, velocity and accelerometer errors, two error metrics are given. For example, $\tilde{r}_{rms}$ refers to the RMS magnitude of the position vector uncertainty, while σ_r refers to the component of the uncertainty along the position vector, $\underline{r}$. It is to be noted that the oscillations in the position and velocity error response are due to the natural oscillations of the trajectory itself. These are eventually damped out because of the closed-loop or feedback nature of the navigation system.

The uncertainty in radial position, σ_r, is reduced to 0.6 km at about 12 hours of flight (48 observations), and thereafter approaches a nearly constant value of 0.44 km. Circumferential position uncertainty, not shown in Figure 5(a), also approaches a nearly constant value of 1.35 km. The slow but steady decrease of $\tilde{r}_{rms}$ is then due to the continuing reduction in the out-of-plane component-see Figure 5(d). There is a similar characteristic for velocity uncertainty shown in Figure 5(b). After 36 hours of flight, the uncertainty in velocity magnitude is reduced to 0.3 m/sec. Figure 5(c) shows how the uncertainty in accelerometer bias is reduced by means of the celestial observations. For example, σ_a is reduced by 70 percent after 36 hours of observation. The improved knowledge of accelerometer bias will continue at an increasing rate corresponding to the accumulated effect of acceleration errors on position. It will be shown later that the eventual reduction in bias uncertainty is 2-3 orders of magnitude for the in-plane accelerometers and 1 order of magnitude for the out-of-plane accelerometer.

4.1.3 Analytical Results for Simplified System Model

Since it is possible to obtain an approximate analytical solution to the near-circular spiral motion of a low-thrust vehicle, it is also possible to find an approximate analytical solution to the navigation problem. The analytical relationships are quite interesting and they help to explain the results obtained from the numerical analysis of the more complex navigation system.

Consider the planar motion of a vehicle under constant thrust acceleration in a central, inverse-square gravitational field. Thrust is directed tangentially, which, for all practical purposes, is equivalent to circumferentially directed thrust. The region of interest here is the near-circular spirals with eccentricities in the range 10^{-4} to 10^{-2}. This region holds true for either the initial phase of the escape spiral or the terminal phase of the capture spiral.

The nonoscillatory or secular terms of vehicle motion may be described by the following approximate solution

$$v_\theta = \left(\mu/r\right)^{1/2} \tag{7}$$

$$V_\theta V_r = 2ra \tag{8}$$

$$\frac{r}{r_0} = \left[\frac{1}{1-\left(\frac{r_0}{\mu}\right)^{1/2} at}\right]^2 \tag{9}$$

$$\theta = \frac{\mu}{4ar_0{}^2}\left[1 - \left(\frac{r_0}{r}\right)^2\right] + \theta_0 \tag{10}$$

where V_θ, V_r, r, and θ are the velocity and position components expressed in a rotating polar coordinate frame. μ is the planet's gravitational constant and a is the thrust acceleration magnitude. Using equations (7) and (8), the linearized differential equations of motion are found to be

$$\delta\dot{V}_\theta = -\delta a \tag{11}$$

$$\delta\dot{V}_r = 12\,\frac{ar}{\mu}\,(r\delta a + a\delta r) \tag{12}$$

$$\delta\dot{\theta} = -\frac{3}{2}\left(\frac{\mu}{r^5}\right)^{1/2}\delta r = \frac{3}{r}\,\delta V_\theta \tag{13}$$

$$\delta\dot{r} = \delta V_r = \left(\frac{r}{\mu}\right)^{1/2}(2r\delta a + 3a\delta r) \tag{14}$$

Although the coefficients in this model are functions of r and, hence, of time, they may be assumed constant (average values could be used) over a period of time during which many navigational observations are made. In this case, a study of navigation accuracy for various types of observation policies may be greatly facilitated by the use of equations (7) - (14).

To illustrate the simplified navigation analysis, suppose that on-board measurements of the in-plane angle between a star (or inertial reference) and the planet are made at intervals of time Δt. The measurement error, n, is assumed to be a zero-mean random variable, independent from one observation to the next, and with variance σ_n^2. Further, let the discrete observation policy be represented by its near-equivalent continuous "white noise" process. Hence, the observation model may be written

$$y = \delta\theta + n \tag{15}$$

$$E\left[n(t)n(t+\lambda)\right] = (\sigma_n^2 \Delta t)\delta(\lambda) = N\delta(\lambda) \tag{16}$$

To complete the simplified model, the deviation in thrust acceleration (or, the accelerometer error) is assumed to be given by a stationary, exponentially correlated random process having a zero mean and variance σ_a^2. The subsidiary equations are then

$$\delta\dot{a} = -\frac{1}{\tau}\delta a + u \tag{17}$$

$$E\left[u(t)u(t+\lambda)\right] = \frac{2}{\tau}\sigma_a^2\ \delta(\lambda) = Q\delta(\lambda) \tag{18}$$

Since V_r and r are related to V_θ through equations (7) and (8), these variables may be neglected in the remaining analysis. The navigation model is therefore represented by

$$\dot{\underline{x}} = F\,\underline{x} + Gu \tag{19}$$

$$y = H\underline{x} + n \tag{20}$$

where

$$\underline{x} \equiv \begin{bmatrix} \delta\theta \\ \delta V_\theta \\ \delta a \end{bmatrix} \tag{21}$$

$$F = \begin{bmatrix} 0 & 3/r & 0 \\ 0 & 0 & -1 \\ 0 & 0 & -1/\tau \end{bmatrix}; \; G = \begin{bmatrix} 0 \\ 0 \\ 1 \end{bmatrix}; \; H = \begin{bmatrix} 1 & 0 & 0 \end{bmatrix} \tag{22}$$

Assuming the observations are processed by the minimum-variance estimation method, the estimation error covariance matrix may be determined from

$$\begin{aligned} \dot{P} &= FP + PF^T - PH^TN^{-1}HP + GQG^T \\ P(0) &= P_0 \end{aligned} \tag{23}$$

Rather than assume a value of P_0 and attempt to solve the above set of nonlinear differential equations, let us consider the "steady-state" solution of (23); i.e., $\dot{P} = 0$. Strictly speaking, the steady state solution can never be obtained exactly since F is not truly constant nor is an infinite time record available. However, if we assume that a large number of observations are made over an interval equal to the system time constant ($\Delta t << \tau$), and that r can be suitably averaged, then the "steady-state" solution should approximate the actual solution of (23). The result for $\dot{P} = 0$ involves the simultaneous solution of 6 nonlinear algebraic equations. An approximate solution of the set of equations is obtained under the assumption $(N/Q)^{1/6} << 2\tau(3/r)^{1/3}$ (Ref. 6). After simplification, the "steady-state" RMS errors are

$$\delta\tilde{\theta}_{RMS} = 2^{7/12} (3/r)^{1/6} \sigma_n^{5/6} \sigma_a^{1/6} \left(\frac{\Delta t^5}{\tau}\right)^{1/12} \tag{24}$$

$$\delta\tilde{V}_{\theta_{RMS}} = 2^{1/4} r^{1/2} \sigma_n^{1/2} \sigma_a^{1/2} \left(\frac{\Delta t}{\tau}\right)^{1/4} \tag{25}$$

$$\delta\tilde{a}_{RMS} = 2^{11/12} \left({}^{r}/{}_{3}\right)^{1/6} \sigma_n^{1/6} \sigma_a^{5/6} \left(\frac{\Delta t}{\tau^5}\right)^{1/12} \tag{26}$$

The most interesting feature of the above results is the power-law dependence of the estimation errors on the navigation parameters (σ_n, Δt) and (σ_a, τ). Thus, for example, (24) tends to verify what one might expect, namely, that $\delta\tilde{\theta}_{RMS}$ is sensitive primarily to the observation error variance, less to the observation interval, and is rather insensitive to acceleration error parameters. The opposite is true for $\delta\tilde{a}_{RMS}$ as seen from (26). In particular, the fact that $\delta\tilde{a}_{RMS}$ varies with such low fractional powers of σ_n and Δt helps to explain why correlated accelerometer errors can be accurately estimated only when the correlation time τ is extremely long - approaching a pure bias error. This was an important result from the previous year's work (Ref. 1), and will again be demonstrated in the next section of this report.

As a numerical example, the following parameters are assumed

$a = 10^{-3}$ m/sec²

$\sigma_a = 2 \times 10^{-5}$ m/sec²

$\tau = 5$ days

$\sigma_n = 0.5$ mrad

$\Delta t = 15$ min

$\mu = 3.986 \times 10^{14}$ m³/sec²

$r_0 = 8230$ km

$r = 8800$ km
(average over 5 days)

From equations (24)-(26), the "steady-state" RMS errors are obtained

$$\delta\tilde{\theta}_{RMS} = 0.206 \text{ mrad}$$

$$\delta\tilde{V}_{\theta_{RMS}} = 0.075 \text{ m/sec}$$

$$\delta\tilde{a}_{RMS} = 0.602 \times 10^{-5} \text{ m/sec}^2$$

To check the "steady-state" solution, the covariance equations (23) were integrated numerically. The following time history was obtained for the velocity and acceleration errors

t	$\delta\tilde{V}_{\theta}$ (RMS)	$\delta\tilde{a}$ (RMS)
0 hours	1.0 m/sec	2.0×10^{-5} m/sec²
2	0.20	1.98
4	0.16	1.78
6	0.14	1.23
8	0.11	0.80
10	0.09	0.65
12	0.08	0.60

Thus, the "steady-state" solution given above is verified and is approached after only 12 hours of flight (48 measurements).

The analytical results of equations (24)-(26) may also be applied to the higher altitude spirals, and in the case where σ_n and Δt are not constant. Thus, as in the digital computer simulation, assume

$$\sigma_n^2 = 2(5 \times 10^{-5}) + \frac{(3200)^2}{r^2 - (6.38 \times 10^6)^2}$$

$$\Delta t = \frac{1}{K} \text{ (Period) } = \frac{2\pi}{K} \left(\frac{r^3}{\mu}\right)^{1/2}$$

As a second example, the following parameters are assumed

$a = 10^{-3}$ m/sec^2 $\qquad \mu = 3.986 \times 10^{14}$ m^3/sec^2

$\sigma_a = 10^{-5}$ m/sec^2 $\qquad r_0 = 50{,}000$ km

$\tau = 5$ days $\qquad r = 55{,}000$ km

$K = 8$ $\qquad \Delta t = 270$ min

$\sigma_n = 0.09$ mrad

$$\left.\begin{array}{l} r = 55{,}000 \text{ km} \\ \Delta t = 270 \text{ min} \\ \sigma_n = 0.09 \text{ mrad} \end{array}\right\} \text{average over 3 days}$$

The "steady-state" errors in the estimates of velocity and acceleration are

$$\delta\tilde{v}_{\theta_{RMS}} = 0.117 \text{ m/sec}$$

$$\delta\tilde{a}_{RMS} = 0.446 \times 10^{-5} \text{ m/sec}^2$$

This solution was found to be in close agreement with numerical results obtained for the non-simplified navigation system model.

4.1.4 Earth Escape From 50,000 km Orbit-Parametric Results

This section of the report describes numerical results obtained from the computer program for the case of Earth-escape navigation initiated from a 50,000 km near-circular orbit. Nominal values for initial position and velocity uncertainty, stellar monitor error, and planet sensor error are listed in Table II. The nominal celestial observation policy consists of measuring the direction to Earth and its subtended angle. These observations are assumed to be made simultaneously at discrete but variable time intervals given by the formula $\Delta t = P/K$ ($\Delta t_{max} = 1$ day), where P is the instantaneous period of the orbit and K is the specified integer number of observations per orbit.

Table III shows the effect of the celestial observation rate on the RMS state estimation errors at the termination of Earth-escape navigation. For this example, a value of 10^{-5} m/sec^2 is assumed for both the high and low frequency components of the accelerometer error. The low frequency component is assumed to be a pure bias ($\tau_{a\ell} = \infty$). It is seen that the observation rate does not have a proportionate effect on the terminal errors, although a significant reduction is obtained for the higher rates. It is interesting, however, that the low data rate of

2/orbit is quite sufficient to hold the in-plane position uncertainty to within 30 km and the in-plane velocity uncertainty to well below 0.1 m/sec. The in-plane accelerometer bias uncertainty is reduced almost three orders-of-magnitude from the initial value of 10^{-5} m/sec^2. A two order-of-magnitude reduction is obtained for the out-of-plane accelerometer.

Table IV shows the effect of the initial accelerometer bias uncertainty on the terminal estimation errors. A celestial observation rate of 8/orbit is assumed. It is noted that about the same results are obtained for accelerometer uncertainties of 10^{-6} and 10^{-5} m/sec^2. This is due to the fact that in each of these cases the bias uncertainty is rapidly reduced to about the same value. The importance of this result is that, if the low-frequency component of accelerometer error is a pure bias, it is not necessary to have an extremely accurate accelerometer. The estimation of the bias provided by the celestial observations would allow a rather poor (1 percent) accelerometer to be used without incurring a serious performance loss.

The effect of observing the Moon under good geometric conditions is illustrated by Figure 6. In this example, the spacecraft approaches the Moon's orbital radius at about 20 days (see Fig. 3), and it is assumed that the timing of the escape spiral is such that the spacecraft comes in close proximity to the Moon. The improvement in position accuracy takes place between 20 and 25 days during which time the spacecraft remains within 100,000 km of the Moon. Thereafter, the position information from the lunar observations becomes less effective in compensating for the accelerometer error - hence, the upturn in the position uncertainty curve. At the escape energy condition, the position uncertainty is 12 km when lunar observations are made as compared to 28 km when they are not. Other runs were made when the lunar observation geometry was rather poor with the result that no significant improvement in navigation accuracy was obtained.

The analytical results given in the previous section of this report indicated that the correlation time of the accelerometer error has a significant effect on navigation accuracy. In particular, when the correlation time is seemingly long but not infinite, it is not possible to obtain an accurate estimate of the accelerometer error and, hence, performance is degraded. This effect is shown in Figures 7(a)-(c) which give the position, velocity and accelerometer error uncertainty as a function of time. The initial uncertainty of both the low and high frequency components of accelerometer error are assumed to be 10^{-6} m/sec^2. Observations of the direction to Earth and its subtended angle are made at the rate of 8 per orbit. Results are shown parametrically for correlation times of 5 days, 100 days, and ∞.

The effect of the finite correlation time begins to show up fairly early, and relatively poorer performance (compared to infinite correlation time) continues throughout the escape spiral. When the correlation time is 5 days, the estimate of accelerometer error shows hardly any improvement. Still, the position and velocity uncertainty at escape are, respectively, 150 km and 0.6 m/sec. The state uncertainties for a 100 day correlation time are, comparatively, a factor of 2 smaller. Table V shows the effect of correlation time in terms of the various components of state uncertainty at the Earth-escape condition.

The relatively poorer performance associated with the finite-time correlation error is a significant result in that it is probably unrealistic to expect the low-frequency accelerometer error to remain constant throughout the entire mission. Rather, this error may be attributed to a slowly changing calibration, perhaps due to component "aging".

4.2 Navigation for Interplanetary Missions

The state estimation uncertainties existing at the termination of the Earth-escape phase are used as initial conditions to investigate the navigation performance for several interplanetary mission examples. Each of these missions include a heliocentric transfer phase and a planet capture (or approach) phase during which the on-board navigation system is assumed to be operable. For the heliocentric transfer phase, celestial observations of both Earth and the target planet are made at fixed time intervals. For the target planetocentric phase, observations are made of the target planet direction and its subtended angle.

Since the accelerometer error correlation time has been shown to have a significant effect on the accuracy of state estimation, it was decided to obtain results for a finite-time correlation in addition to the pure bias error. For descriptive purposes only, the two values of correlation are designated by the terms System I and System II accelerometers.

$$\left.\begin{array}{ll} \text{System I Accelerometer:} & \tau_{a\ell} = \infty \text{ (bias)} \\ \text{System II Accelerometer:} & \tau_{a\ell} = 100 \text{ days} \end{array}\right\rangle \sigma_{a\ell} = 10^{-6} \text{ m/sec}$$

To reiterate, the initial state estimation errors for each of these accelerometers are obtained from the termination of Earth-escape as given by Figures 7(a)-(c). Results for the interplanetary missions are discussed below in terms of the accuracy of position estimation. Additional results are summarized in Tables VI - IX.

4.2.1 Mars Orbiter Mission

The trajectory profile for this mission consists of a 205.4 day heliocentric transfer and rendezvous with Mars followed by a low-thrust capture spiral down to a 10,000 km circular orbit around Mars. Constant thrust propulsion along with an optimal steering program and optimal coast period are assumed for the heliocentric transfer phase which is illustrated in Figure 8. This diagram shows the Earth, vehicle, and Mars position at various times in the flight. Also shown is the direction of the applied thrust.

Figure 9 shows the time history of position uncertainty during the heliocentric transfer. The maximum errors associated with the System I and II accelerometers are respectively, 1000 km and 3000 km. The respective errors at Mars rendezvous are 300 km and 1500 km. The initial error buildup is due principally to the uncertainty in the low frequency component of the accelerometer error. This is eventually damped by the celestial position information. The dip in the curves at mid flight is due to the combined effect of an improved celestial observation geometry, and the coast period during which the accelerometers are turned off. Results show that the largest components of position uncertainty lie in the plane of motion.

Figure 10 shows the position uncertainty during the Mars-capture phase, again, the initial state uncertainties being taken from the termination of the heliocentric rendezvous. It is seen that the position estimate is continuously improved with time (there are small oscillations similar to the escape spiral but a smooth curve is used for simplicity of presentation). For all practical purposes, the accelerometer correlation time has little effect on navigation accuracy after a few days of planet observations. The final position uncertainty in the 10,000 km orbit is less than 1 km.

4.2.2 Venus Orbiter Mission

The trajectory profile for this mission consists of a 120 day heliocentric transfer and rendezvous with Venus followed by a low-thrust capture spiral down to a 20,000 km circular orbit around Venus. A diagram of the rendezvous trajectory is given by Figure 11. Here, thrust is applied continuously (no coast period) with optimal magnitude and direction. Figures 12 and 13 show the time history of position uncertainty during the heliocentric and capture phases. The characteristic and numerical values are similar to the Mars Orbiter Mission.

4.2.3 Mars Flyby Mission

The heliocentric phase of this mission is diagrammed in Figure 14. The transfer trajectory takes 120 days and assumes an optimum, variable thrust mode of propulsion. The hyperbolic approach velocity at Mars is 12.6 km/sec and the distance of closest approach is specified as 6500 km. It should be made clear that the vehicle does not continue to thrust during the planetocentric approach, but, rather, "free-falls" towards Mars.

The heliocentric position uncertainty shown in Figure 15 displays a characteristic similar to the Mars Orbiter Mission. The principal difference occurs at the end of the heliocentric phase where, in the case of flyby, the position uncertainty is not reduced until the last day or so. The reason for this lies in the fact that the vehicle approaches the orbit of Mars at high velocity and, therefore, spends relatively little time in the near vicinity of Mars where position information can be improved. To compensate for this, the observation interval should be reduced as Mars is approached. Figure 16 shows the effect of reducing the observation interval to 1/2 hour during the planetocentric approach. Position uncertainty is presented in terms of the closest approach distance rather than the full vector uncertainty, $\tilde{r}_{rms}$. The initial uncertaintites are 850 km and 1950 km corresponding to the System I and System II accelerometers. A few observations bring the uncertainty down to 100 km in each case. Thereafter, the System I accuracy is significantly better up until the last observation which occurs 1 hr before closest approach. The final uncertainty is about 5 km. The reason for the large deviation between the System I and System II curves is due to the poorer quality initial velocity information in the later case - 0.8 m/sec as compared to 0.1 m/sec. The velocity uncertainty is not improved by additional celestial observations. The reason that accelerometer correlation time is relatively less significant for the low-thrust capture spiral (see Fig. 10) is simply that this type of trajectory allows much improvement in the velocity information.

4.2.4 Jupiter Flyby Mission

This mission assumes a 360 day transfer using an optimum, variable thrust program as pictured in Figure 17. The hyperbolic approach velocity at Jupiter is 28.3 km/sec and the distance of closest approach is 138,000 km (about 2 Jupiter radii). As in the Mars example, the planetocentric trajectory is non-thrusted.

Spacecraft position during the heliocentric transfer to Jupiter is not too well determined as seen from Figure 18. This is true in terms of an absolute kilometer measure, but it must be remembered that the distances involved here are considerably greater than in the Mars mission. A rapid improvemnt in position information is obtained as the vehicle closes on Jupiter during the last 5 days of flight. Figure 19 shows this improvement for a reduced observation interval of 2 hrs. In this example, the linear uncertainty in Jupiter's apparent diameter was arbitrarily taken as 32 km. The initial condition for the approach navigation is taken at 355 days of the heliocentric transfer at which time the vehicle's 12.5 million kilometers from Jupiter and has an uncertainty in the distance of closest approach of 4400 km (System I) and 42,000 km (System II). At the end of 2 days, these uncertainties are reduced to 200 km and 1000 km, respectively. The final observation is made at a distance of 0.5×10^6 km, 4 hrs before closest approach. At this time, the RMS uncertainty in the closest approach distance is of the order 50-80 km.

4.3 Effect of Incorrect A Priori Covariance

The method of minimum variance estimation requires knowledge of the a priori statistics which characterize the assumed error model. Generally, these statistics will not be known exactly, but one must proceed anyway with the best assumption available at the time. Under these circumstances, it could be said that the state estimation procedure is really only conditionally optimal. That is, the estimate is optimal only under the conditions that the assumed statistics are the true statistics. When this is not satisfied, the state estimate is not optimal nor is the computed statistics of the estimation error equal to the true statistics of this error. The first question concerning optimality will not be given further consideration here. However, the second question concerning the computed estimation errors is of practical interest. That is, how do the true and computed errors compare when incorrect a priori covariance data are used in the state estimation procedure? Some answers to this question are given in the following paragraphs.

The a priori information enters the problem in four ways: (1) P_o, the error covariance matrix of the initial state estimate, (2) U, the matrix of "white noise" covariances which are used to model the correlated noise process, (3) A, the linearized system matrix which contains the noise correlation time constants, and (4) N_k, the covariance matrix of the random observation errors at time t_k. Errors or uncertainty in the a priori information are designated ΔP_o, ΔU, ΔA and ΔN_k, respectively. It is of interest, then, to determine $\Delta P_k \equiv P_k^* - P_k$, where P_k is the <u>computed</u> state estimation error covariance obtained under the assumption that the a priori data are correct, and P_k^* is the true error covariance obtained from the estimation procedure which uses the incorrect a priori data.

It can be shown that the difference between the true and computed covariance at the time of an observation is given by the equation (using notation of Reference 1)

$$\Delta P_k = (I-K_kM_k)\Delta P_k'(I-K_kM_k)^T + K_k\Delta N_kK_k^T \tag{27}$$

where $\Delta P_k'$ is the error propagated from the previous observation time which may be obtained from the solution of the differential equation

$$\begin{aligned}\Delta\dot{P} &= A\Delta P + \Delta PA^T + B\Delta UB^T \\ &\quad + \Delta A(P+\Delta P) + (P+\Delta P)\Delta A^T\end{aligned} \tag{28}$$

with t in the interval (t_{k-1}, t_k) and with the initial condition $\Delta P\ (t_{k-1})$. The above equations are included in the computer program and, upon option, ΔP_k may be computed for arbitrary values of ΔP_o, ΔU, ΔA and ΔN.

Some numerical results which show the effect of incorrect a priori covariance assumptions are given in Tables X - XIV. The reference trajectory for these examples is the Earth-escape spiral from a 50,000 km near-circular orbit which has been described earlier in this report. Eight observations per orbit are assumed.

Incorrect Initial Velocity Covariance

The effect of an assumed initial velocity covariance that is smaller than the true value is virtually insignificant. Results were obtained for a true error of 2 m/sec and 10 m/sec when the assumed value was 1 m/sec. In each case, the true state estimation errors approached the computed errors after only 6 observations (1 day of flight). The explanation of this result is that the velocity information provided by the celestial observations is accurate to within a small fraction of 1 m/sec, and, therefore, the larger initial velocity errors are quickly negated.

Table X compares the computed and true estimation errors when the assumed initial velocity uncertainty is 1 m/sec but the true uncertainty is zero. In this case, the true estimation errors are smaller, although the difference is not very significant over most of the flight. At t = 25 days, the true estimation errors are about 30-35 percent less than the computed values.

Incorrect Accelerometer Bias Covariance

Table XI shows the effect on state estimation when the true accelerometer bias uncertainty is twice the assumed value. In this case, the true estimation errors, and in particular $\tilde{a}^*_{rms}$, are larger than the computed values. However, the position and velocity estimates converge after only 3 days of flight. This result seems to be in contradiction to the fact that true accelerometer bias uncertainty remains significantly larger than the computed value until about 20 days of flight. The explanation is that the quantities listed are the magnitudes of the estimation error *vectors*, and, in the case of accelerometer bias, the out-of-plane component is the principal contributor to the total error. Actually, convergence of the in-plane components of $\tilde{a}_{rms}$ and $\tilde{a}^*_{rms}$ occurs at 4 days of flight.

Table XII compares the computed and true estimation errors when the assumed accelerometer bias uncertainty is 10 times larger than the true value. The effect on position and velocity estimation is similar to the case where the assumed initial velocity covariance was too large. That is, the true estimation errors are smaller than the computed errors, but not significantly so throughout most of the flight. The last two columns of Table XII show the gradual convergence trend of the computed and true uncertainties in the accelerometer bias.

Incorrect Correlation Time of Accelerometer Error

Results previously described in Figures 7(a)-(c) indicated the sensitivity of navigation accuracy to the correlation time constant of the low-frequency component of accelerometer error. A similar sensitivity is found when the assumed correlation time is incorrect. Table XIII compares the computed and true estimation errors when the accelerometer error is actually correlated (τ = 100 days) but assumed to be a bias. In this case, at least initially, it is possible for the true estimation errors in position and velocity to be smaller than the computed errors. This is because the "free" system (no estimation) is basically less sensitive to a correlated error than it is to a bias. However, as time progresses, the true estimation errors become larger than the computed values. This is because the true error in estimating the acceleration is always larger than the computed error, and, in fact, the difference grows with time. In other words, correlated noise cannot be as accurately estimated as bias noise. At t = 25 days, the true estimation errors are larger by a factor of 3-5.

Table XIV shows the effect of assuming the accelerometer error to be correlated (τ = 100 days) when it is actually a bias. In this case, the true estimation errors are always smaller and become significantly so as time progresses.

The following table summarizes the limited results obtained to date and indicates a possible means of choosing which value of τ to assume.

TRUE POSITION ESTIMATION ERRORS
NEAR EARTH-ESCAPE, KM

Assumed, τ → True, τ^* ↓	∞	100	5
∞	23	40	55
100	77	61	Not Computed 61< <105
5	167	Not Computed 105< <167	105

Suppose that the true value of τ is completely unknown and might take on any one of a discrete set of values. In this case it might be best to choose that value of τ which gives the smallest maximum error. Among the limited choices in the above table, the best choice might then be $\tau = 5$ since this column has the smallest maximum value (105 km). Of course, this value is about 5 times larger than the minimum error obtained when $\tau = \tau^* = \infty$. A further improvement in the best choice would be possible given some probability distribution of τ. In this case, the best choice could be based on a weighted average criterion or, possibly, a minimum probability of exceeding a specified error tolerance. As a simple example, suppose that $P(\infty) = 0.25$, $P(100) = 0.75$, $P(5) = 0$ and that the error tolerance is 50 km. Then, either of the above criteria would lead to a choice of $\tau = 100$.

5. CONCLUDING REMARKS

The specific numerical results described in this report should best be considered indicative of the performance that may be expected of celestial-inertial navigation systems applied to low-thrust spacecraft. Final performance results could only be obtained after such systems are actually designed and tested so that improved instrumentation error models are available for analysis. However, an attempt was made in this study (see also Ref. 1) to assign reasonable characteristics and numerical values to the assumed error model, or, if this was not possible, to investigate the error model sensitivity by parameter variations. Given this type of analysis, then, it can be fairly concluded that an on-board celestial-inertial system utilizing optimal state estimation techniques will offer high performance navigation for future interplanetary missions. This means, essentially, that (1) the state estimation errors over the entire flight are maintained at low enough levels to be consistent with fuel-efficient methods of trajectory control or guidance, and (2) the terminal estimation errors are probably well within most mission requirements.

There is no intent in this analysis to imply that celestial-inertial systems are the only means of obtaining high performance navigation for spacecraft under continuous, low-thrust acceleration. For example, if one could accurately model the expected thrust fluctuations from nominal conditions, or if one could assure that these fluctuations are so small as to be insignificant, then it would be possible to eliminate the on-board accelerometers. Also, Earth-based tracking of unmanned spacecraft might eliminate the need for the on-board system, or parts of it, but probably at the expense of frequent tracking operations in order to effectively monitor the thrust acceleration.

APPENDIX

LIST OF SYMBOLS

General

a	thrust acceleration magnitude
A, B	linearized system matrices, $\dot{\underline{x}} = A\underline{x} + B\underline{u}$
K	filter or weighting matrix for observations
M	celestial observation geometry matrix
N	covariance matrix of celestial sensor random errors
P	covariance matrix of state estimation errors
U	covariance matrix of "white noise" inputs, $\underline{u}$
$\sigma^2_{a\ell}, \sigma^2_{ah}$	variances of low and high frequency components of accelerometer error
σ^2_n	variance of planet sensor error
σ^2_R	variance of planet horizon uncertainty
σ^2_η	variance of stellar monitor error
$\tau_{a\ell}, \tau_{ah}$	correlation time constants of low and high frequency components of accelerometer error
τ_η	correlation time constant of stellar monitor error

Estimation Error Metrics

$\tilde{r}_{rms}, \tilde{V}_{rms}, \tilde{a}_{rms}$	RMS values of the vector-magnitude errors in estimating, respectively, the position, velocity and low-frequency component of accelerometer error; obtained from the square-root of the trace of the respective covariance sub-matrices.
$\sigma_r, \sigma_V, \sigma_a$	RMS components of the estimation error vectors along the nominal position, velocity and acceleration vectors, respectively.

REFERENCES

1. Friedlander, A., "Analysis of an Optimal Celestial-Inertial Navigation Concept for Low-Thrust Interplanetary Vehicles". NASA CR-457, May 1966.

2. Kalman, R., "A New Approach to Linear Filtering and Prediction Problems". Journal of Basic Engineering, Trans. ASME, Vol. 82, No. 1, March 1960.

3. Smith, G., Schmidt, S. and McGee, L., "Application of Statistical Filter Theory to the Optimal Estimation of Position and Velocity On Board a Circumlunar Vehicle". NASA TR-135, 1962.

4. White, J., Callas, G., and Cicolani, L., "Application of Statistical Filter Theory to the Interplanetary Navigation and Guidance Problem". NASA TN D-2697, 1965.

5. Friedlander, A., "Analysis of Guidance Perturbations for a Low-Thrust Mars Orbiter Mission Using SNAP-8". NASA TN d-1433, 1962.

6. Breakwell, J., "Theory of Minimum Effort Control", Final Report on Contract No. NAS 1-3777, pp. 3.1-46, Aug. 1965.

Table I

PRINCIPAL EFFECTS OF OBLATENESS AND THRUST ON ORBITAL MOTION

ORBITAL ELEMENT	OBLATENESS SECOND HARMONIC ONLY, $J_{\oplus} = 1.62\times10^{-3}$	THRUST ACCELERATION a, TANGENTIALLY DIRECTED
RADIAL DISTANCE OR SEMI-AXIS	$r = r_0 + J\left(\frac{R_E^2}{r}\right)\sin^2 i \cos(2\eta + 2\omega)$	$r = r_0\left[\frac{1}{1-\left(\frac{r_0}{\mu}\right)^{1/2}at}\right]^2$
ECCENTRICITY	$e = e_0 + \frac{1}{2}J\left(\frac{R_E}{r}\right)^2\Big[(2-3\sin^2 i)\cos\eta$ $+\frac{1}{2}\sin^2 i\cos(\eta+2\omega)+\frac{7}{6}\sin^2 i\cos(3\eta+2\omega)\Big]$	$\dot{e} = 2\left(\frac{r}{\mu}\right)^{1/2}(e+\cos\eta)a$ $e = \frac{2a}{\mu}r^2 : e_0 = \cos\eta_0 = \frac{2a}{\mu}r_0^2$
ARGUMENT OF PERICENTER	$\omega = \omega_0 + \frac{J}{e}\left(\frac{R_E}{r}\right)^2\Big\{\sin\eta - \sin^2 i\Big[\frac{3}{2}\sin\eta$ $+\frac{1}{4}\sin(\eta+2\omega) - \frac{7}{12}\sin(3\eta+2\omega)\Big]\Big\}$	$\mathring{\omega} = 2\left(\frac{r}{\mu}\right)^{1/2}\frac{\sin\eta}{e}a$ $\omega = \omega_0 + Nt : e_0 = \cos\eta_0 = \frac{2a}{\mu}r_0^2$ $N = \left(\frac{\mu}{r^3}\right)^{1/2}$ MEAN ANGULAR MOTION
LONGITUDE OF ASCENDING NODE	$\Omega = \Omega_0 - J\left(\frac{R_E}{r}\right)^2\cos i\,(Nt)$	$\Omega = \Omega_0$
INCLINATION	$i = i_0 + \frac{1}{4}J\left(\frac{R_E}{r}\right)^2\sin 2i\cos 2(\eta+\omega)$	$i = i_0$

R_E = EQUATORIAL RADIUS OF EARTH

μ = GRAVITATIONAL CONSTANT OF EARTH

η = TRUE ANAMOLY = $\theta - \omega$

θ = POLAR ANGLE $\approx \theta_0 + Nt$ (SHORT TERM

Table II

NOMINAL ERROR PARAMETER VALUES

1. Initial Position and Velocity Uncertainty

Position (x, y, z) = 1 km (RMS)

Velocity (x, y, z) = 1 $^{m}/sec$ (RMS)

Correlation = 0

2. Accelerometer Errors

a) Low frequency: $\sigma_{a\ell} = 10^{-6}$ m/sec² (or 10^{-5})

$\tau_{a\ell} = \infty$ (bias)

b) High frequency: $\sigma_{ah} = 10^{-6}$ m/sec² (or 10^{-5})

τ_{ah} = 30 minutes

3. Stellar Monitor Error

σ_{η} = 10 sec arc

τ_{η} = 30 minutes

4. Planet Sensor Error (random)

σ_{η} = 10 sec arc

σ_{R} = 3.2 km (horizon uncertainty)

Table III

EFFECT OF CELESTIAL OBSERVATION RATE ON RMS STATE ESTIMATION ERRORS AT EARTH-ESCAPE CONDITIONS

NOTE: For this example, $\sigma_a = 10^{-5}$ m/sec^2

OBSERVATION RATE / STATE VARIABLE	2/ORBIT	8/ORBIT	16/ORBIT
Radial Position (KM)	20	12	9
Angular Position (SEC ARC)	10	7	5
Radial Velocity (M/SEC)	0.05	0.03	0.02
Tangential Velocity (M/SEC)	0.03	0.02	0.01
Plane Orientation (SEC ARC)	12	11	8
Accelerometer Bias In-Plane Out-Of-Plane (M/SEC^2)	3×10^{-8} 3×10^{-7}	2×10^{-8} 2×10^{-7}	1.5×10^{-8} 1.4×10^{-7}

Table IV

EFFECT OF ACCELEROMETER BIAS MAGNITUDE ON RMS STATE ESTIMATION ERRORS AT EARTH-ESCAPE CONDITIONS

ACCELEROMETER BIAS / STATE VARIABLE	0	10^{-6} M/Sec^2	10^{-5} M/Sec^2
Radial Position (KM)	1.5	11	12
Angular Position (SEC ARC)	2	5	7
Radial Velocity (M/SEC)	0.005	0.02	0.03
Tangential Velocity (M/SEC)	0.003	0.01	0.02
Plane Orientation (SEC ARC)	2	6	11
Accelerometer Bias In-Plane Out-Of-Plane (M/SEC^2)	 0 0	 1.7×10^{-8} 1×10^{-7}	 2×10^{-8} 2×10^{-7}

Table V

EFFECT OF ACCELEROMETER ERROR CORRELATION TIME
RMS STATE ESTIMATION ERRORS AT EARTH-ESCAPE CONDITIONS

CORRELATION TIME / STATE VARIABLE	∞ (BIAS)	100 DAYS	5 DAYS
Radial Position (KM)	11	75	144
Angular Position (SEC ARC)	5	10	10
Radial Velocity (M/SEC)	0.02	0.3	0.5
Tangential Velocity (M/SEC)	0.01	0.2	0.4
Plane Orientation (SEC ARC)	6	10	12
Accelerometer Error In-Plane Out-Of-Plane (M/SEC)	1.7×10^{-8} 1×10^{-7}	4×10^{-7} 3.4×10^{-7}	0.98×10^{-6} 0.89×10^{-6}

Table VI

SUMMARY OF STATE ESTIMATION ERRORS FOR MARS ORBITER MISSION

STATE ESTIMATION ERRORS	SYSTEM I ACCELEROMETER	SYSTEM II ACCELEROMETER
Termination of Earth-Escape Phase		
$\tilde{r}_{rms}$, km	28	84
$\tilde{v}_{rms}$, $^{m}/sec$	0.06	0.31
$\tilde{a}_{rms}$, $^{m}/sec$	1.2×10^{-7}	6.6×10^{-7}
Termination of Heliocentric Phase		
$\tilde{r}_{rms}$	311	1510
$\tilde{v}_{rms}$	0.17	1.13
$\tilde{a}_{rms}$	0.29×10^{-7}	8.8×10^{-7}
Termination of Mars-Capture Phase		
$\tilde{r}_{rms}$	0.6	1.1
$\tilde{v}_{rms}$	0.13	0.19
$\tilde{a}_{rms}$	0.26×10^{-7}	6.3×10^{-7}

Table VII

SUMMARY OF STATE ESTIMATION ERRORS FOR VENUS ORBITER MISSION

STATE ESTIMATION ERRORS	SYSTEM I ACCELEROMETER	SYSTEM II ACCELEROMETER
Termination of Earth-Escape Phase		
$\tilde{r}_{rms}$, km	28	84
$\tilde{v}_{rms}$, $^{m}/sec$	0.06	0.31
$\tilde{a}_{rms}$, $^{m}/sec^{2}$	1.2×10^{-7}	6.6×10^{-7}
Termination of Heliocentric Phase		
$\tilde{r}_{rms}$	220	1020
$\tilde{v}_{rms}$	0.18	1.1
$\tilde{a}_{rms}$	0.28×10^{-7}	9.1×10^{-7}
Termination of Venus-Capture Phase		
$\tilde{r}_{rms}$	0.8	1.3
$\tilde{v}_{rms}$	0.15	0.20
$\tilde{a}_{rms}$	0.27×10^{-7}	6.3×10^{-7}

Table VIII

SUMMARY OF STATE ESTIMATION ERRORS FOR MARS FLYBY MISSION

STATE ESTIMATION ERRORS	SYSTEM I ACCELEROMETER	SYSTEM II ACCELEROMETER
Termination of Earth Escape Phase		
$\tilde{r}_{rms}$, km	28	84
$\tilde{v}_{rms}$, $^{m}/sec$	0.06	0.31
$\tilde{a}_{rms}$, $^{m}/sec^2$	1.2×10^{-7}	6.6×10^{-7}
Termination of Heliocentric Phase		
$\tilde{r}_{rms}$	900	2100
$\tilde{v}_{rms}$	0.3	1.6
$\tilde{a}_{rms}$	0.29×10^{-7}	10.5×10^{-7}
Mars Closest Approach		
$\tilde{r}_{rms}$	43	47
$\tilde{v}_{rms}$	3.3	3.7

Table IX

SUMMARY OF STATE ESTIMATION ERRORS FOR JUPITER FLYBY MISSION

STATE ESTIMATION ERRORS	SYSTEM I ACCELEROMETER	SYSTEM II ACCELEROMETER
Termination of Earth-Escape Phase		
$\tilde{r}_{rms}$, km	28	84
$\tilde{v}_{rms}$, $^m/sec$	0.06	0.31
$\tilde{a}_{rms}$, $^m/sec^2$	1.2×10^{-7}	6.6×10^{-7}
Termination of Heliocentric Phase		
$\tilde{r}_{rms}$	8900	86,000
$\tilde{v}_{rms}$	0.69	10.7
$\tilde{a}_{rms}$	0.22×10^{-7}	14×10^{-7}
Jupiter Closest Approach		
$\tilde{r}_{rms}$	320	370
$\tilde{v}_{rms}$	44	50

Table X

ESTIMATION ERRORS WITH INCORRECT INITIAL VELOCITY COVARIANCE

Assumed Velocity Covariance, 1 m/sec

* True Velocity Covariance, 0

t days	$\tilde{r}_{rms}$ km	$\tilde{r}^*_{rms}$ km	$\tilde{V}_{rms}$ m/sec	$\tilde{V}^*_{rms}$ m/sec	$\tilde{a}_{rms}$ 10^{-6} m/sec^2	$\tilde{a}^*_{rms}$ 10^{-6} m/sec^2
0	1.7	1.7	1.73	1.73	1.73	1.73
1	5.7	5.7	0.27	0.27	1.69	1.69
2	4.8	4.7	0.19	0.16	1.12	1.09
3	4.5	4.2	0.16	0.14	1.03	1.01
4	4.4	4.0	0.13	0.11	0.94	0.92
5	4.3	3.8	0.12	0.10	0.90	0.88
10	5.4	4.5	0.07	0.06	0.70	0.69
15	8.4	6.6	0.06	0.05	0.48	0.47
20	15.0	11.4	0.06	0.04	0.27	0.25
25	23.0	15.2	0.06	0.04	0.14	0.10

Table XI

ESTIMATION ERRORS WITH INCORRECT ACCELEROMETER BIAS COVARIANCE

Assumed Bias, $\sigma_{a\ell} = 10^{-6}$ m/sec²

True Bias, $\sigma^{*}_{a\ell} = 2\times10^{-6}$ m/sec²

t days	$\tilde{r}_{rms}$ km	$\tilde{r}^{*}_{rms}$ km	$\tilde{V}_{rms}$ m/sec	$\tilde{V}^{*}_{rms}$ m/sec	$\tilde{a}_{rms}$ 10^{-6} m/sec²	$\tilde{a}^{*}_{rms}$ 10^{-6} m/sec²
0	1.7	1.7	1.73	1.73	1.73	3.46
1	5.7	6.4	0.27	0.35	1.69	3.32
2	4.8	5.5	0.19	0.21	1.12	1.99
3	4.5	4.5	0.16	0.16	1.03	1.83
4	4.4	4.4	0.13	0.13	0.94	1.68
5	4.3	4.3	0.12	0.12	0.90	1.62
10	5.4	5.4	0.07	0.07	0.70	1.09
15	8.4	8.4	0.06	0.06	0.48	0.61
20	15.0	15.0	0.06	0.06	0.27	0.28
25	23.0	23.0	0.06	0.06	0.14	0.14

Table XII

ESTIMATION ERRORS WITH INCORRECT ACCELEROMETER BIAS COVARIANCE

Assumed Bias, $\sigma_{a\ell} = 10^{-6}$ m/sec²

True Bias, $\sigma^*_{a\ell} = 10^{-7}$ m/sec²

t days	$\tilde{r}_{rms}$ km	$\tilde{r}^*_{rms}$ km	$\tilde{V}_{rms}$ m/sec	$\tilde{V}^*_{rms}$ m/sec	$\tilde{a}_{rms}$ 10^{-6} m/sec²	$\tilde{a}^*_{rms}$ 10^{-6} m/sec²
0	1.7	1.7	1.73	1.73	1.73	0.17
1	5.7	5.4	0.27	0.23	1.69	0.40
2	4.8	4.3	0.19	0.17	1.12	0.54
3	4.5	4.1	0.16	0.14	1.03	0.49
4	4.4	3.9	0.13	0.11	0.94	0.45
5	4.3	3.8	0.12	0.10	0.90	0.44
10	5.4	4.4	0.07	0.04	0.70	0.44
15	8.4	6.5	0.06	0.03	0.48	0.41
20	15.0	11.3	0.06	0.02	0.27	0.23
25	23.0	15.1	0.06	0.02	0.14	0.10

Table XIII

ESTIMATION ERRORS WITH INCORRECT CORRELATION TIME OF ACCELEROMETER ERROR

Assumed Correlation, $\tau_{a\ell} = \infty$

True Correlation, $\tau^*_{a\ell}$ = 100 Days

t days	$\tilde{r}_{rms}$ km	$\tilde{r}^*_{rms}$ km	$\tilde{V}_{rms}$ m/sec	$\tilde{V}^*_{rms}$ m/sec	$\tilde{a}_{rms}$ 10^{-6} m/sec^2	$\tilde{a}^*_{rms}$ 10^{-6} m/sec^2
0	1.7	1.7	1.73	1.73	1.73	1.73
1	5.7	5.7	0.27	0.27	1.69	1.69
2	4.8	4.7	0.19	0.18	1.12	1.12
3	4.5	4.2	0.16	0.14	1.03	1.03
4	4.4	4.1	0.13	0.11	0.94	0.96
5	4.3	4.0	0.12	0.10	0.90	0.94
10	5.4	5.7	0.07	0.08	0.70	0.81
15	8.4	12.4	0.06	0.13	0.48	0.70
20	15.0	31.7	0.06	0.22	0.27	0.64
25	23.0	76.6	0.06	0.33	0.14	0.68

Table XIV

ESTIMATION ERRORS WITH INCORRECT CORRELATION TIME OF ACCELEROMETER ERROR

Assumed Correlation, $\tau_{a\ell} = 100$ days

True Correlation, $\tau^*_{a\ell} = \infty$

t days	$\tilde{r}_{rms}$ km	$\tilde{r}^*_{rms}$ km	$\tilde{V}_{rms}$ m/sec	$\tilde{V}^*_{rms}$ m/sec	$\tilde{a}_{rms}$ 10^{-6} m/sec^2	$\tilde{a}^*_{rms}$ 10^{-6} m/sec^2
0	1.7	1.7	1.73	1.73	1.73	1.73
1	5.7	5.7	0.27	0.27	1.69	1.69
2	4.8	4.8	0.20	0.19	1.12	1.12
3	4.6	4.5	0.17	0.16	1.03	1.03
4	4.6	4.4	0.15	0.13	0.98	0.94
5	4.7	4.3	0.14	0.12	0.96	0.90
10	7.2	6.1	0.13	0.09	0.80	0.70
15	13.5	11.0	0.15	0.10	0.66	0.49
20	28.0	21.4	0.19	0.11	0.58	0.29
25	61.0	40.0	0.27	0.14	0.62	0.20

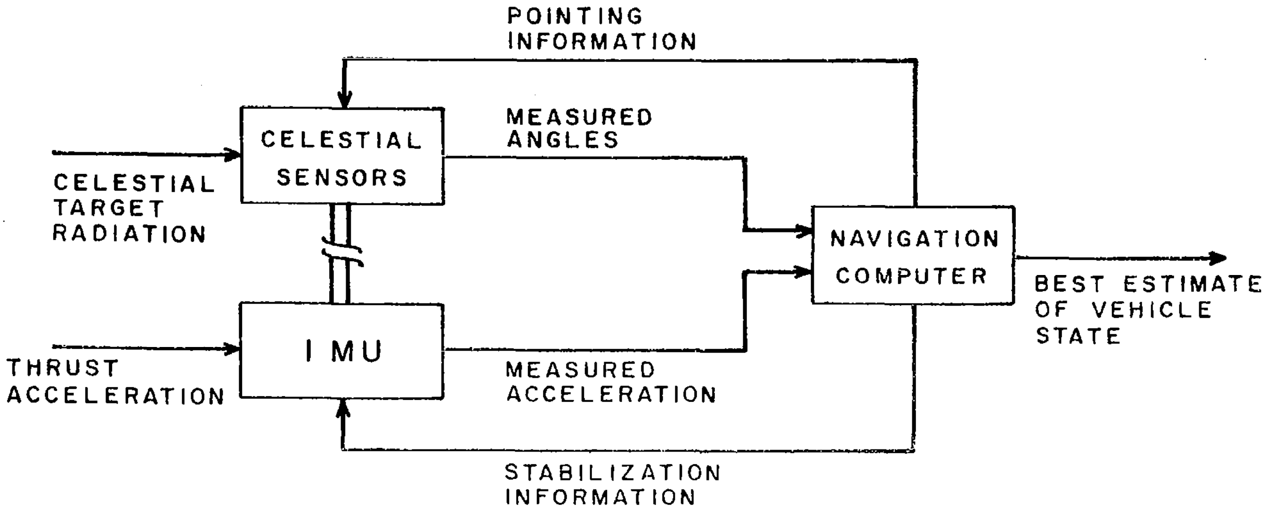

(a) CELESTIAL-INERTIAL NAVIGATION SYSTEM

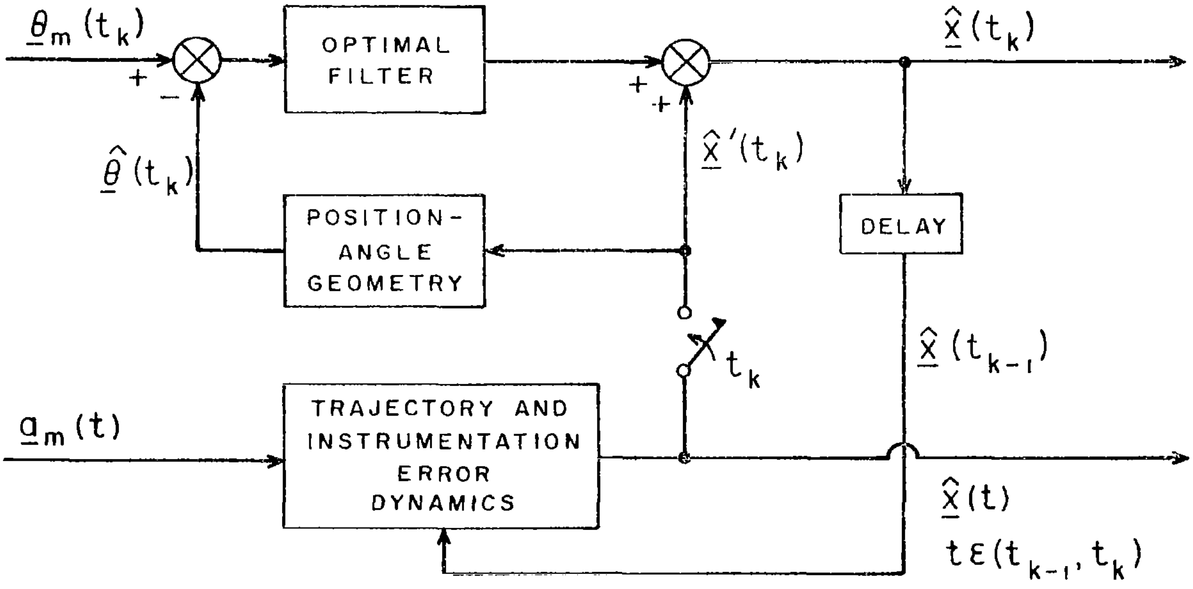

(b) NAVIGATION COMPUTER

FIGURE 1

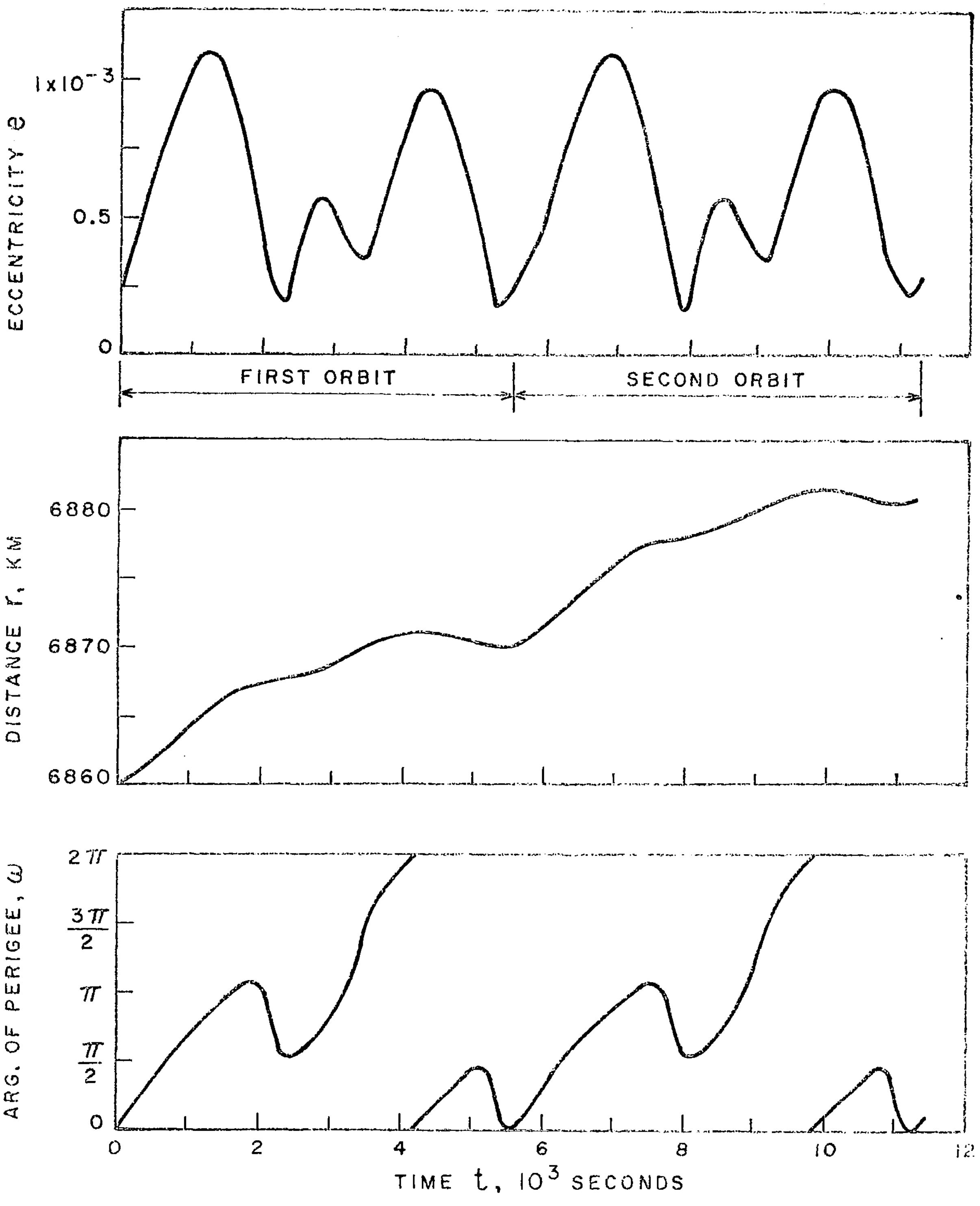

FIGURE 2 VARIATION OF ORBITAL ELEMENTS FOR LOW THRUST SPIRAL ABOUT OBLATE EARTH

$a=10^{-3} m/sec^2$, $i_o=45°$

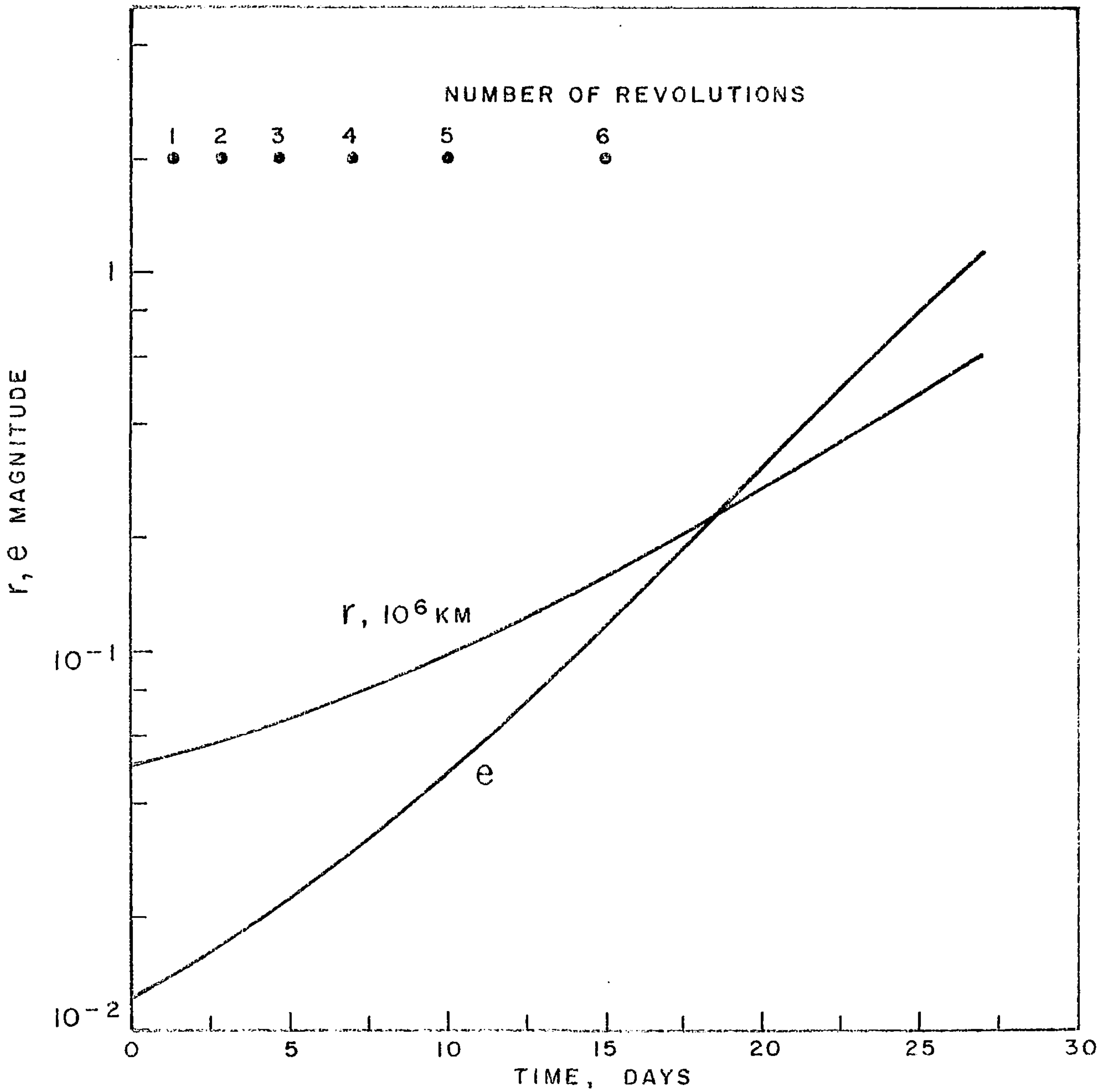

FIGURE 3 RADIAL DISTANCE AND ECCENTRICITY ALONG NOMINAL EARTH ESCAPE TRAJECTORY

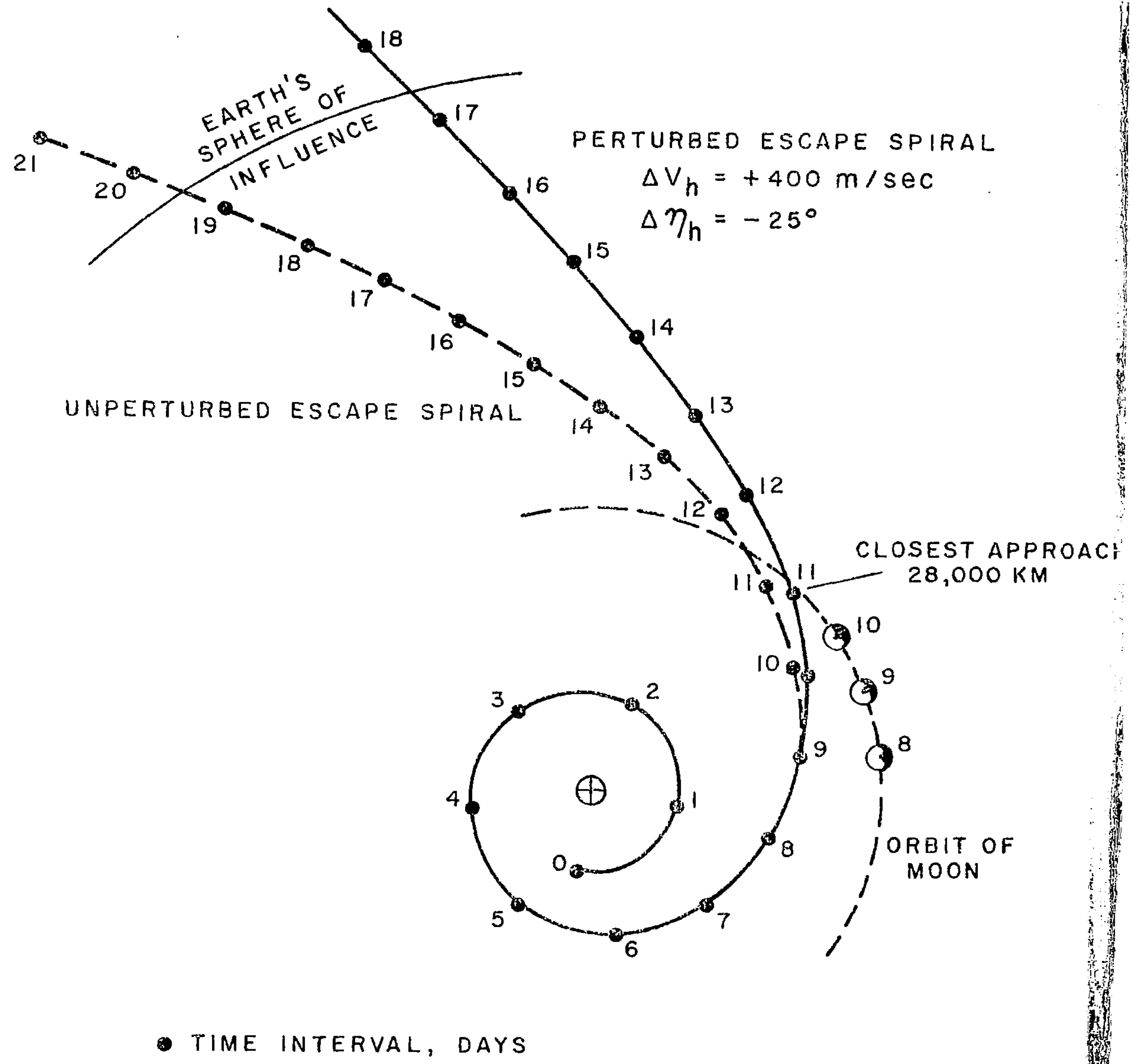

FIGURE 4 PERTURBING EFFECT OF MOON ON LOW-THRUST ESCAPE SPIRAL

$a=10^{-3}$ m/sec^2 $\quad i-i_{☽} = 3°$

$\Omega-\Omega_{☽} = -5°$

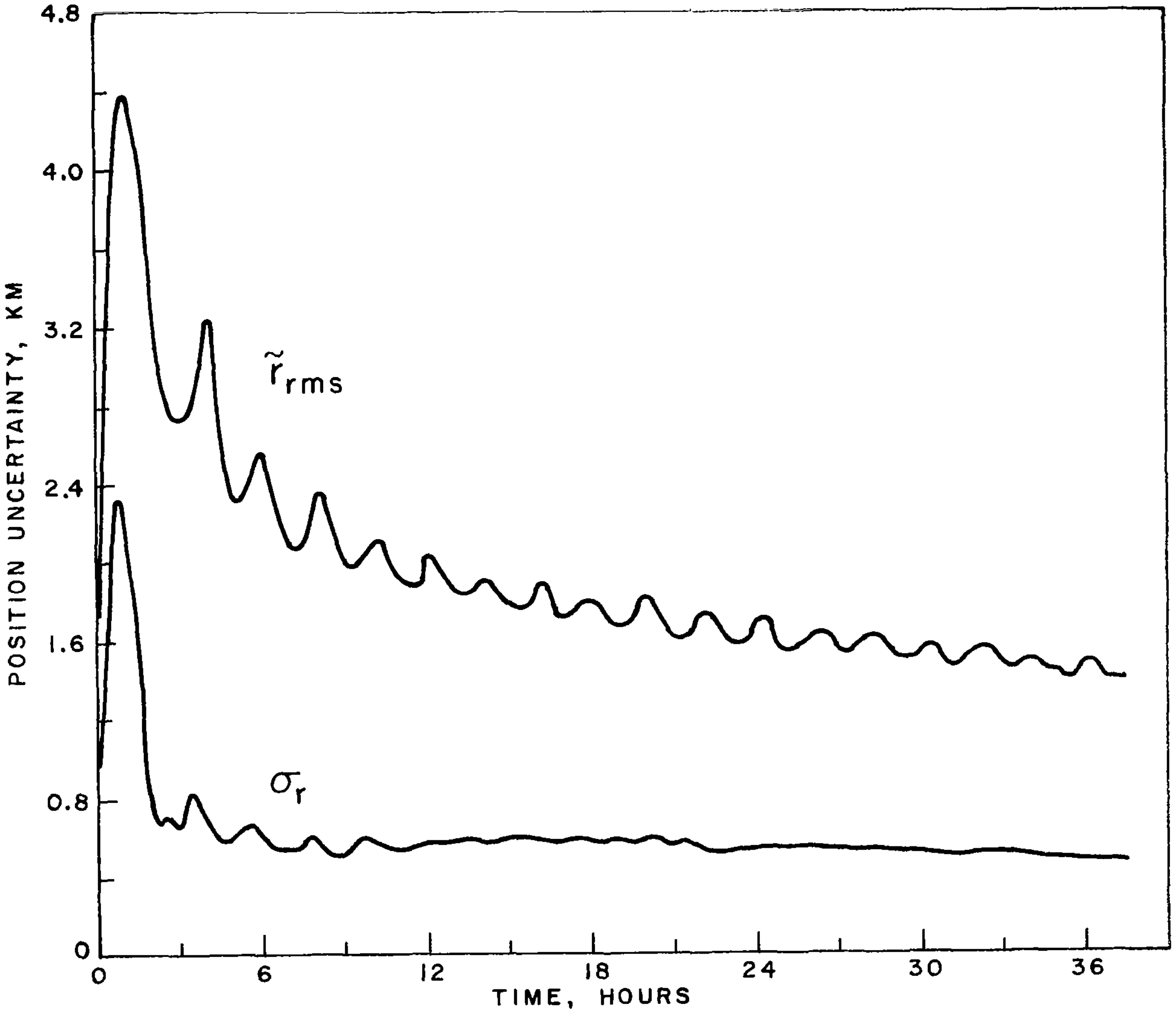

a) POSITION UNCERTAINTY

FIGURE 5 TIME HISTORY OF STATE ESTIMATION ERRORS DURING EARLY PART OF EARTH ESCAPE SPIRAL, START FROM 8230 KM ORBIT, a = 10^{-3} m/sec^2

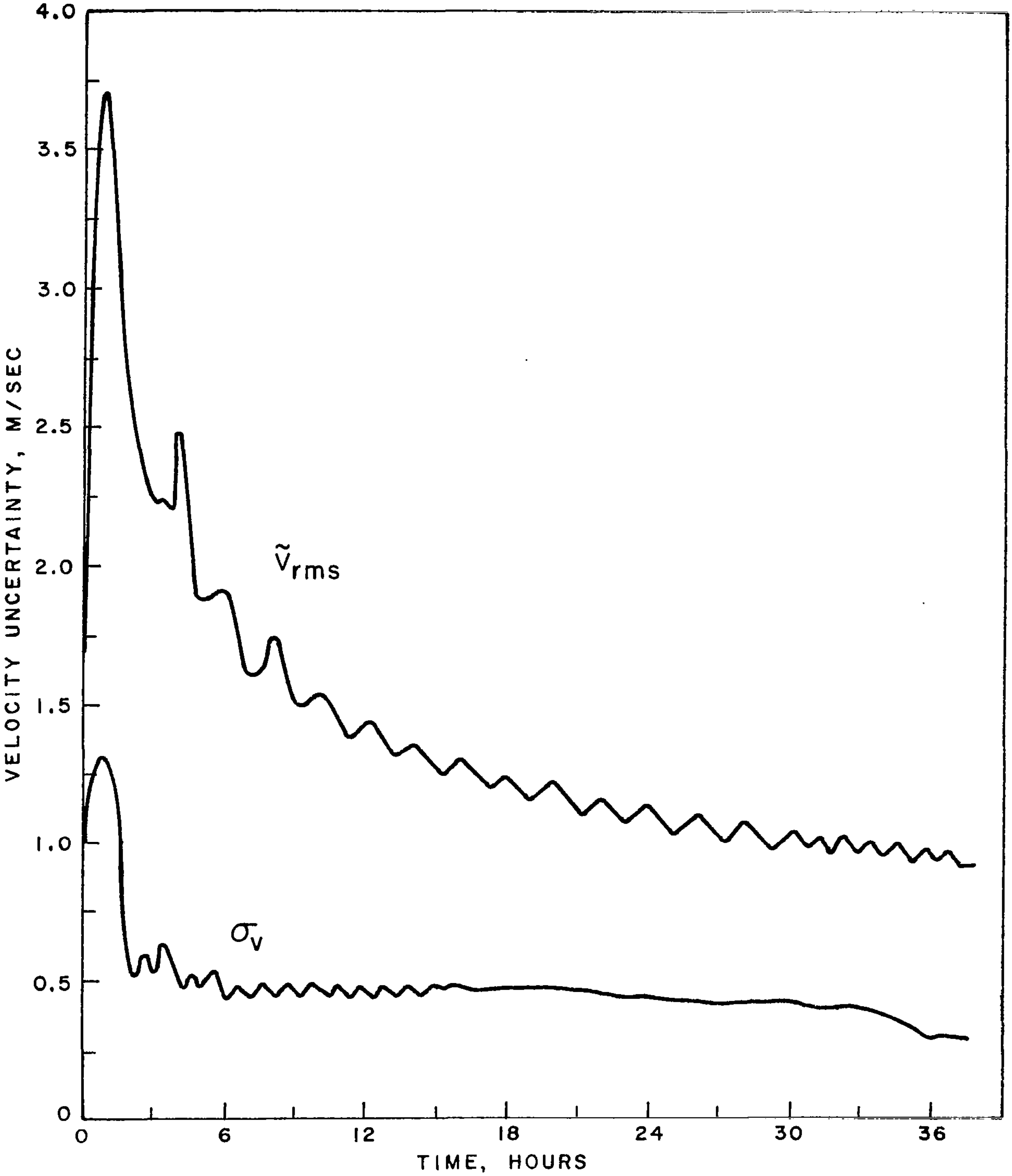

b) VELOCITY UNCERTAINTY

FIGURE 5 CONTINUED

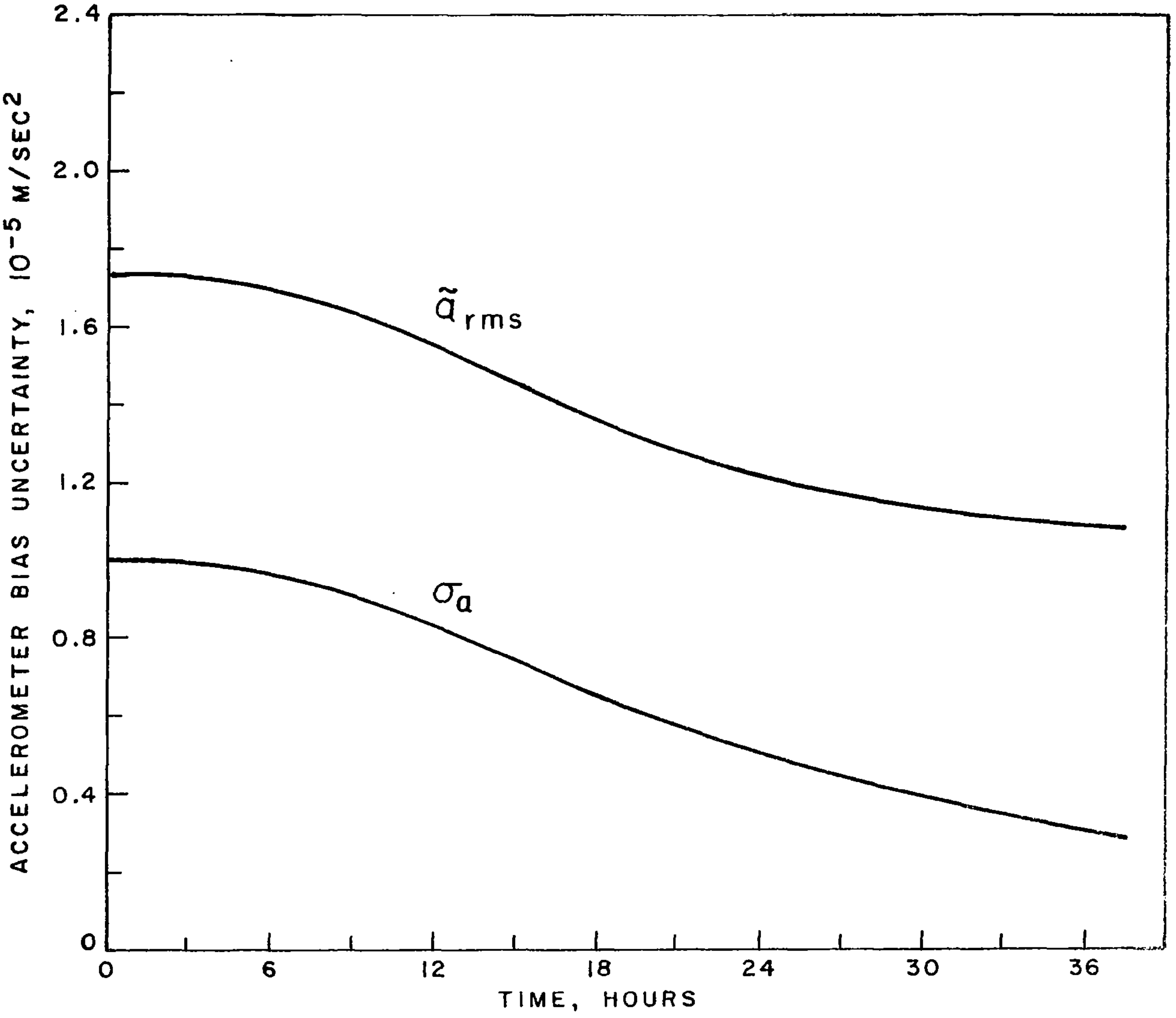

c) ACCELEROMETER BIAS UNCERTAINTY

FIGURE 5 CONTINUED

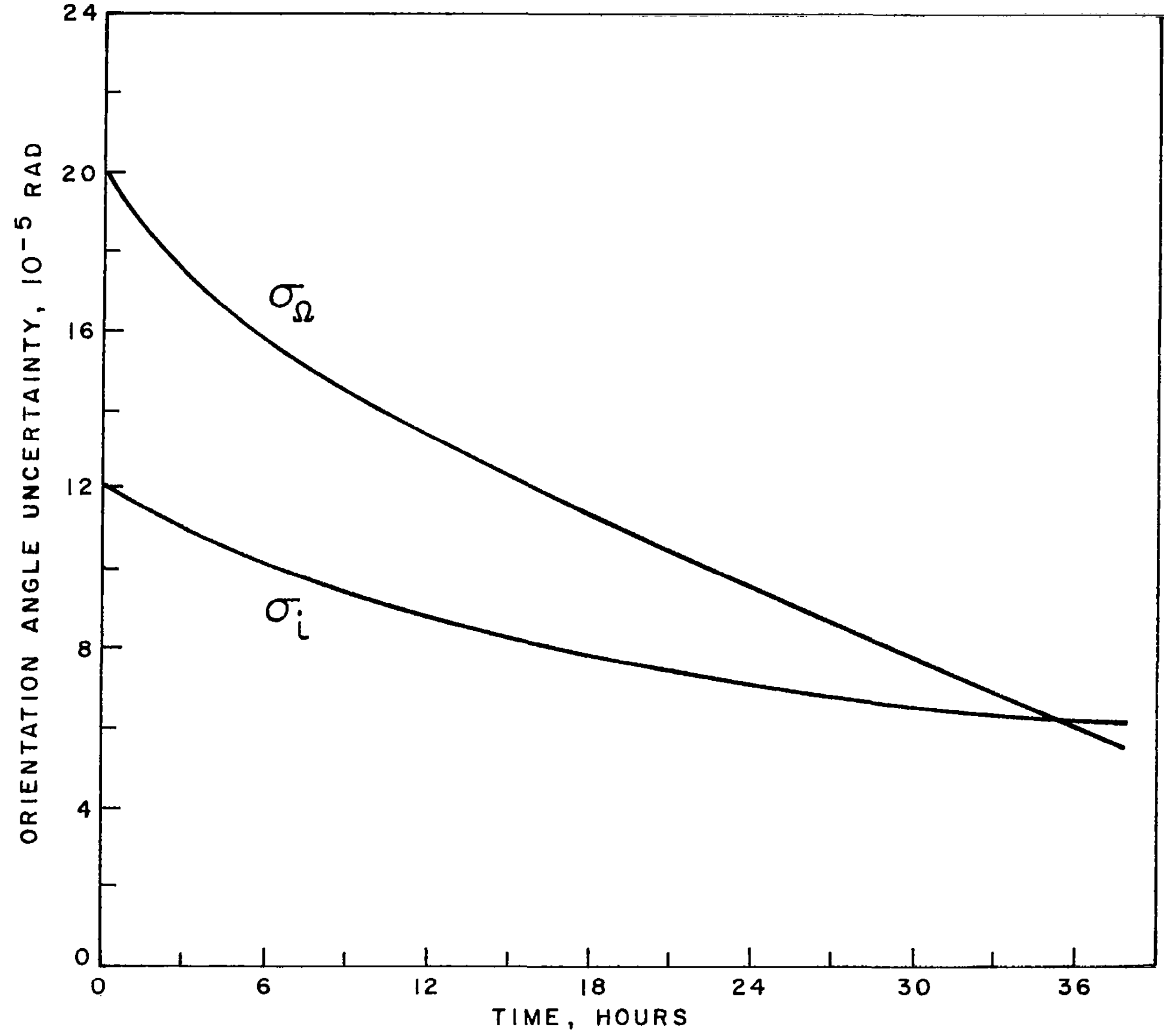

d) LONGITUDE OF ASCENDING NODE AND INCLINATION UNCERTAINTY

FIGURE 5 CONTINUED

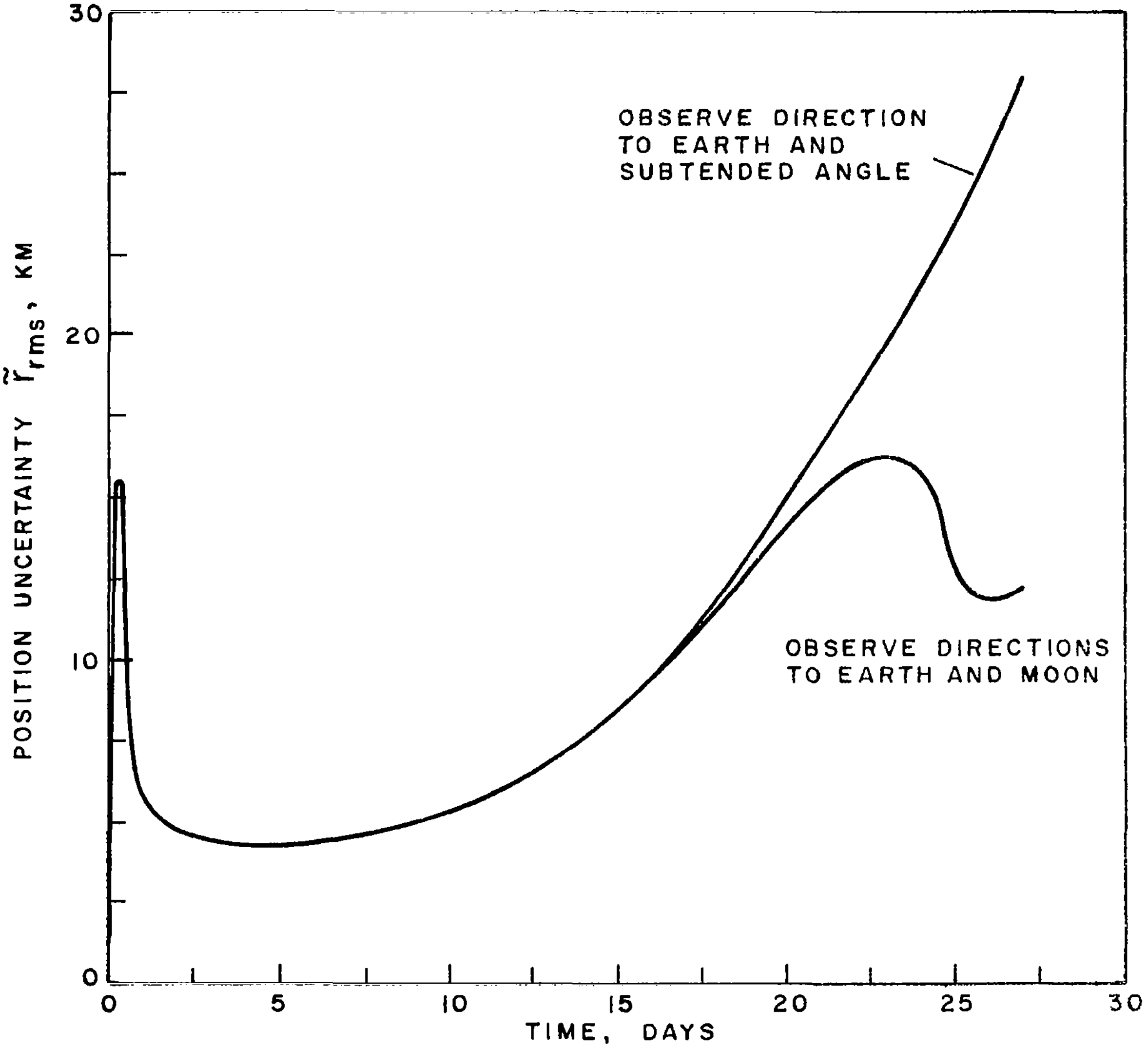

FIGURE 6 EFFECT OF LUNAR OBSERVATIONS ON NAVIGATION ACCURACY, EARTH ESCAPE PHASE FROM 50,000 KM ORBIT

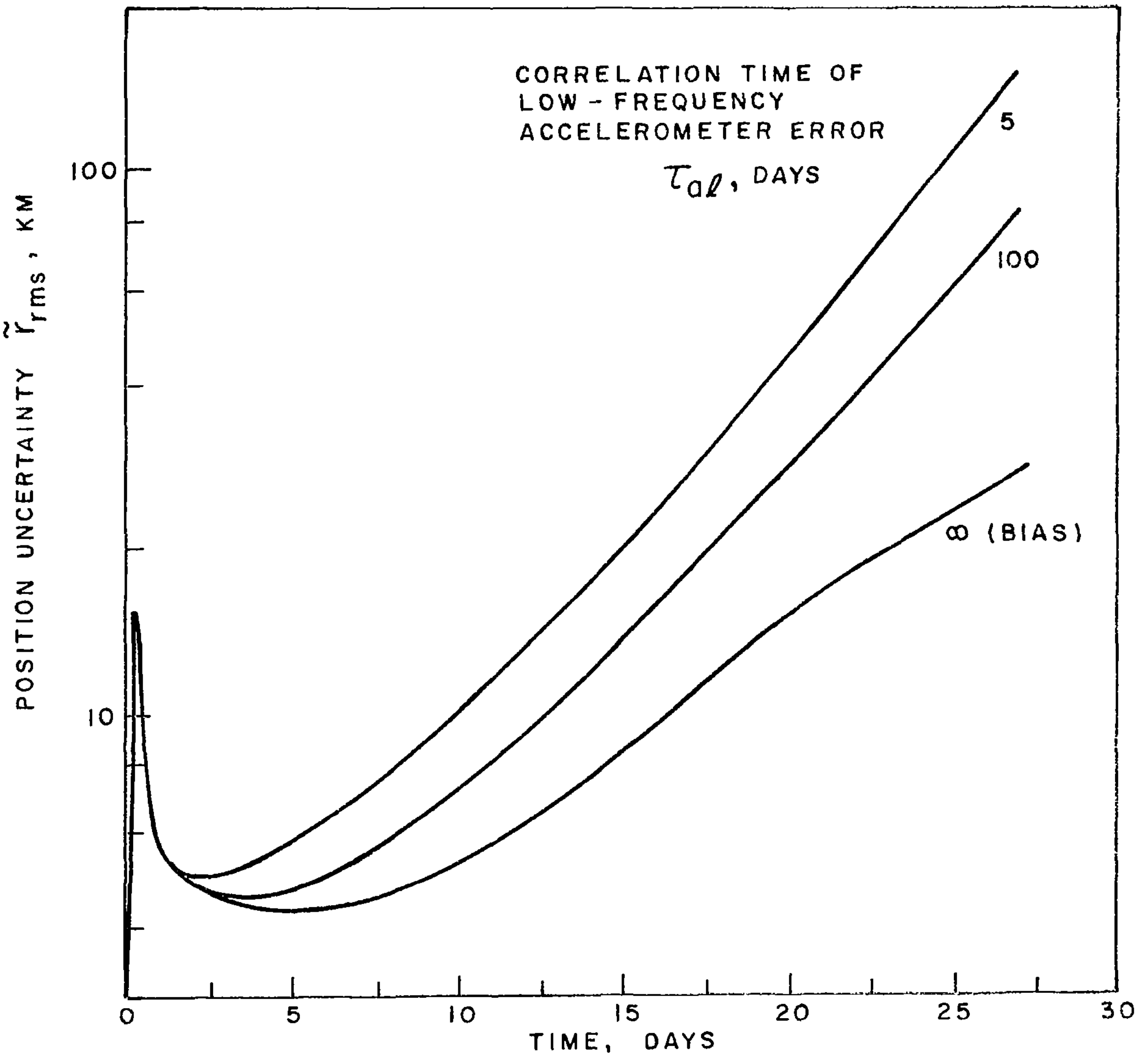

a) POSITION UNCERTAINTY

FIGURE 7 EFFECT OF ACCELEROMETER CORRELATION TIME ON NAVIGATION ACCURACY, EARTH ESCAPE PHASE FROM 50,000 KM ORBIT

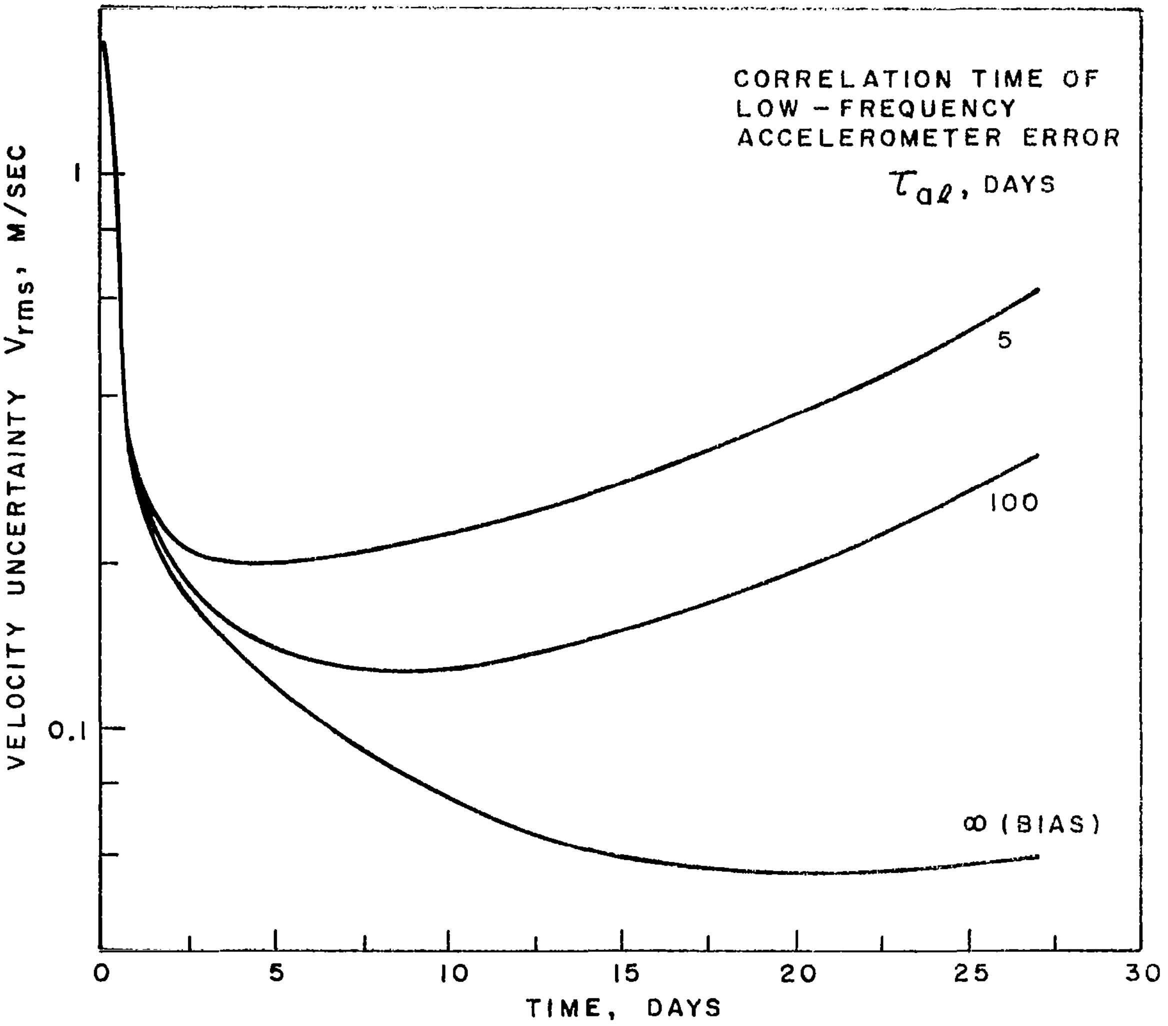

b) VELOCITY UNCERTAINTY

FIGURE 7 CONTINUED

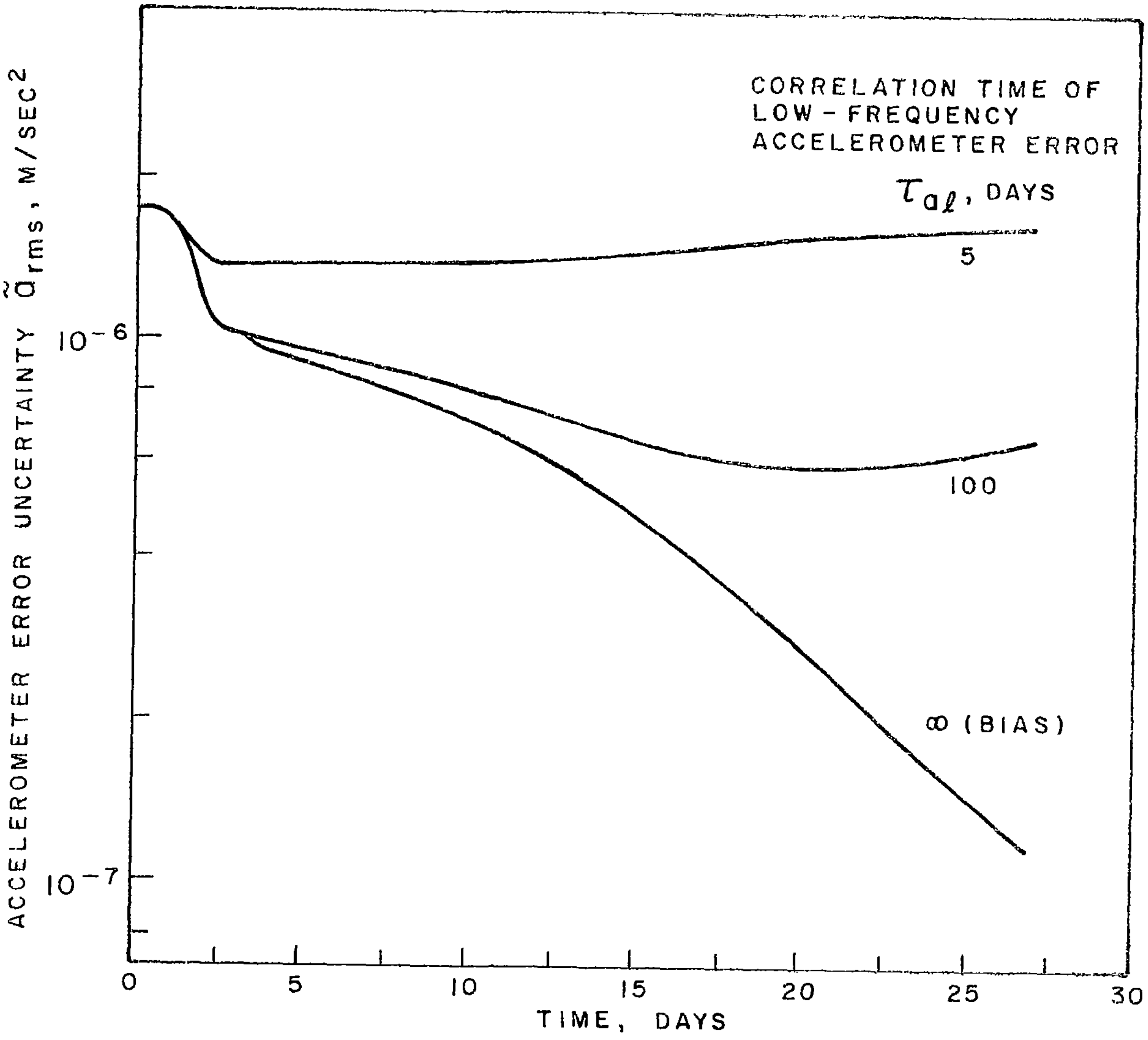

c) LOW-FREQUENCY ACCELEROMETER ERROR UNCERTAINTY

FIGURE 7 CONTINUED

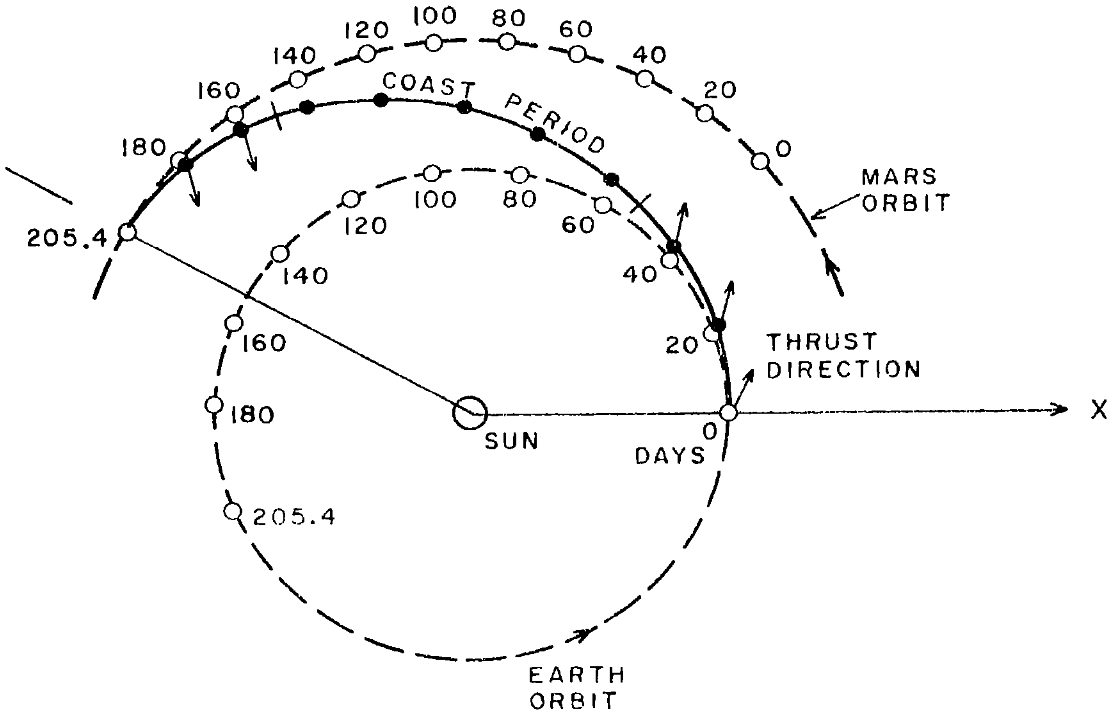

FIGURE 8 MARS RENDEZVOUS 205.4 DAYS, CONSTANT THRUST MODE WITH COAST PERIOD

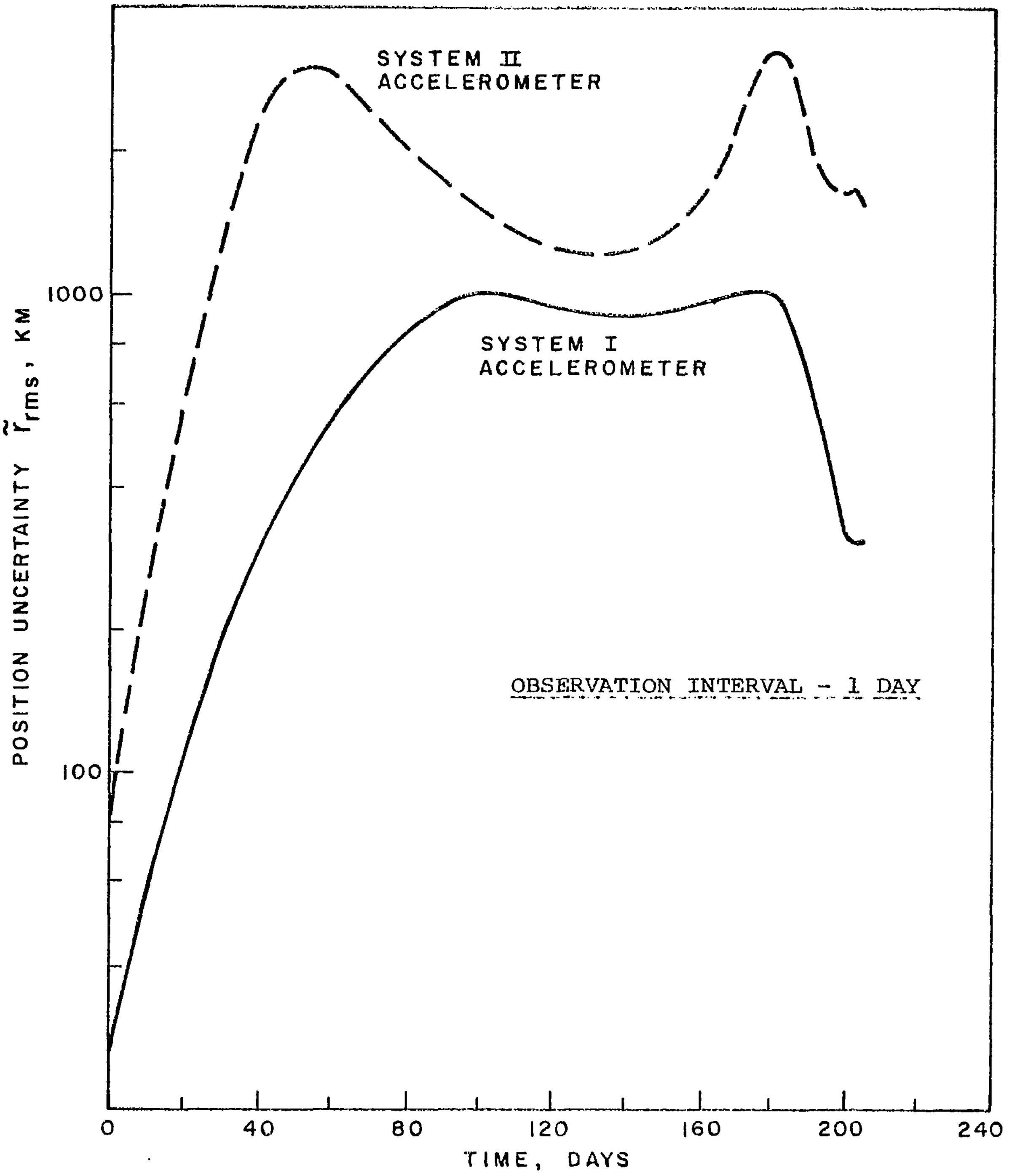

FIGURE 9 POSITION UNCERTAINTY DURING HELIOCENTRIC PHASE, MARS ORBITER MISSION

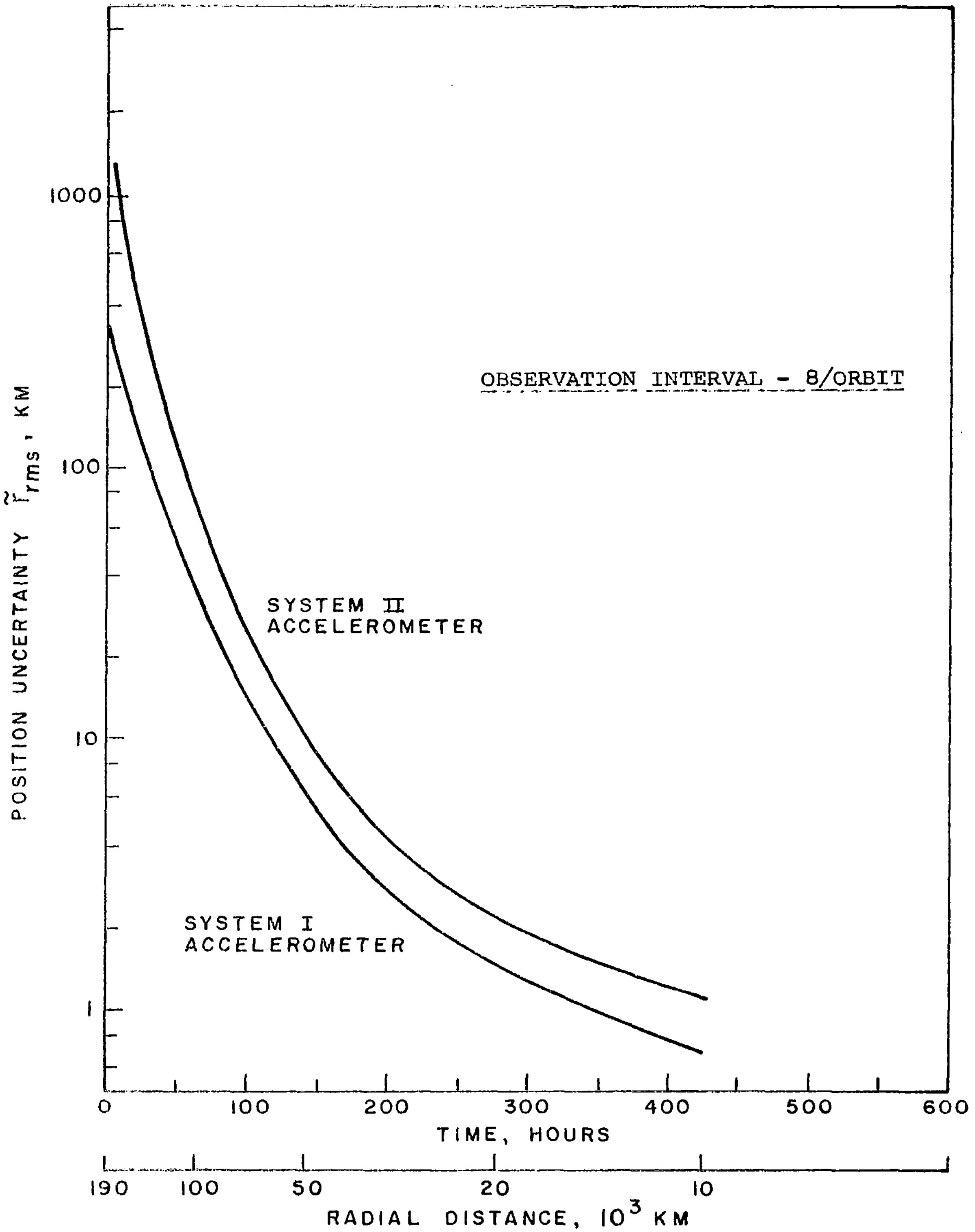

FIGURE 10 POSITION UNCERTAINTY DURING MARS CAPTURE PHASE, MARS ORBITER MISSION

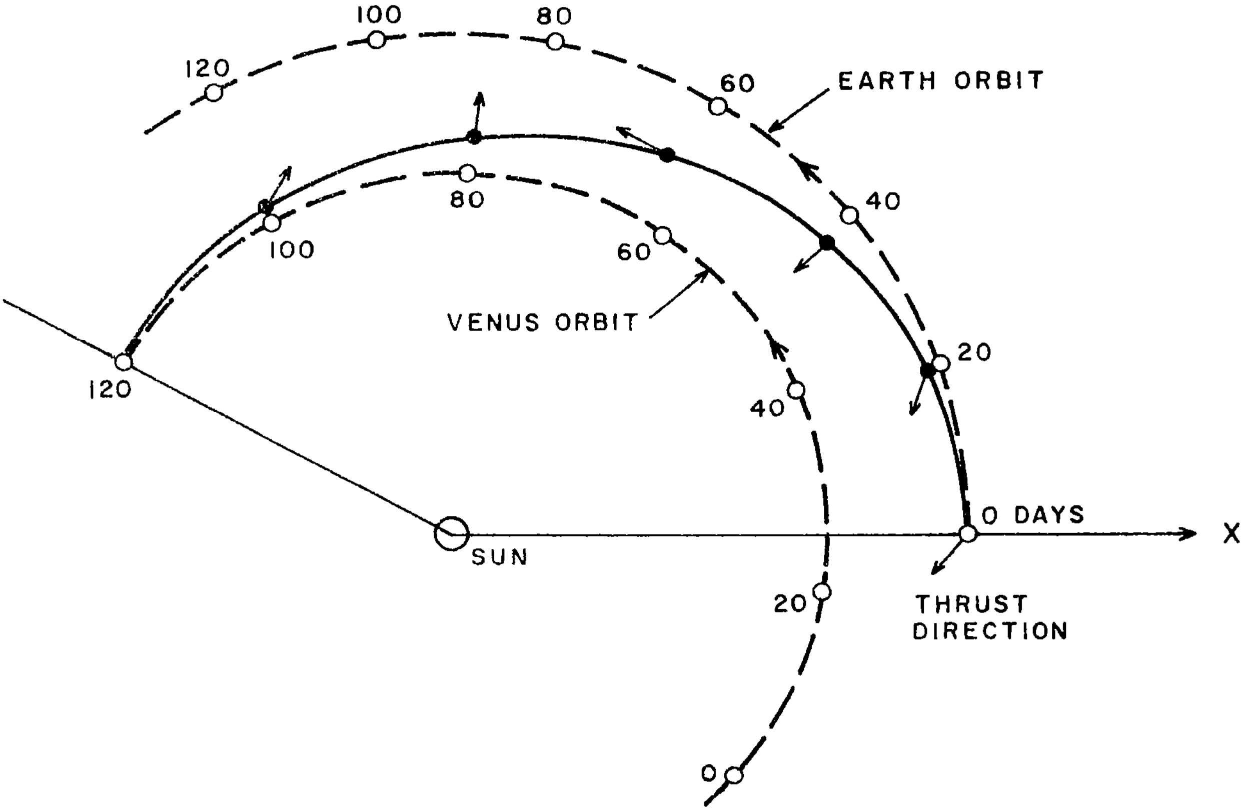

FIGURE 11 VENUS RENDEZVOUS 120 DAYS, VARIABLE THRUST MODE

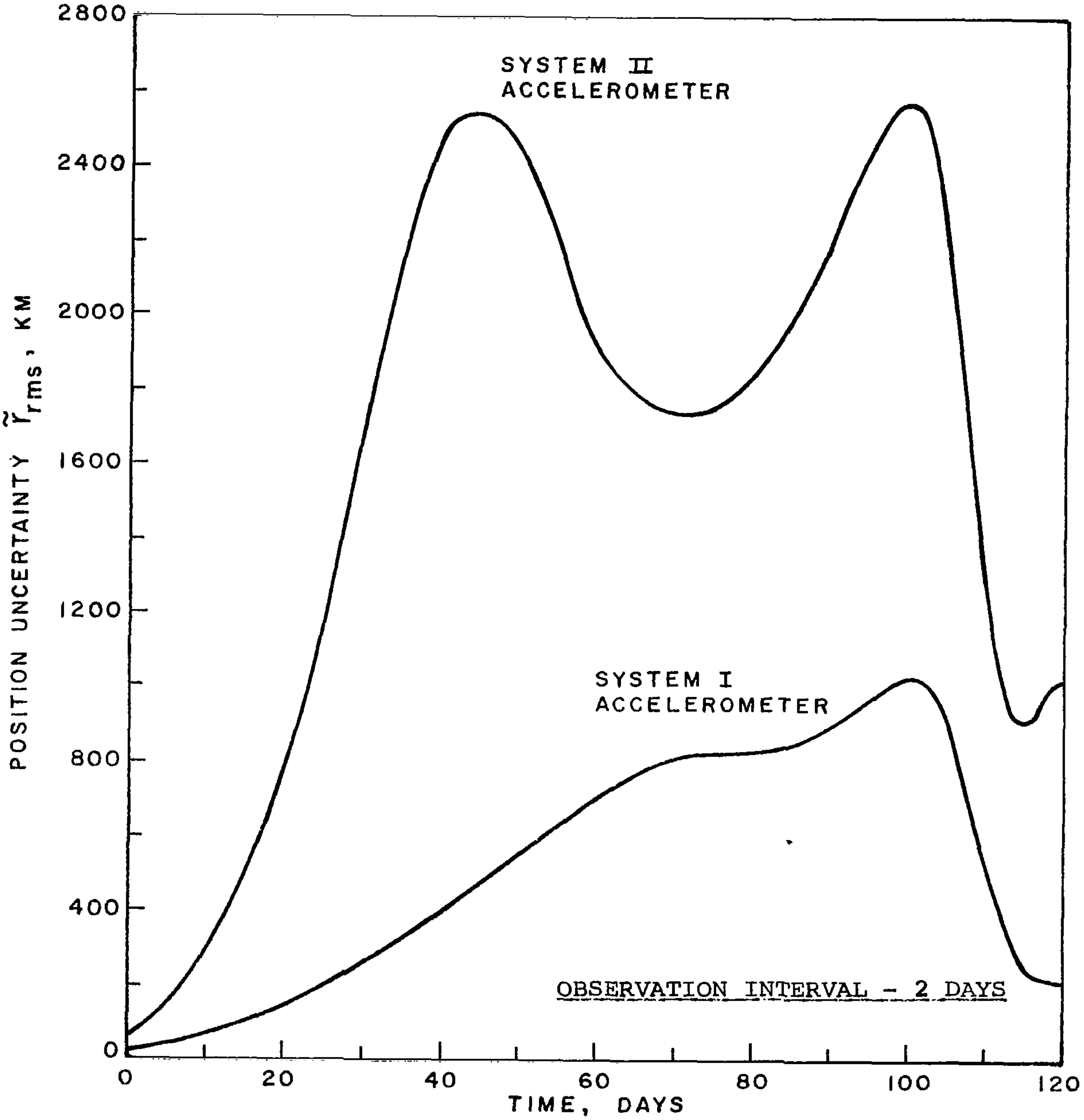

FIGURE 12 POSITION UNCERTAINTY DURING HELIOCENTRIC PHASE, VENUS ORBITER MISSION

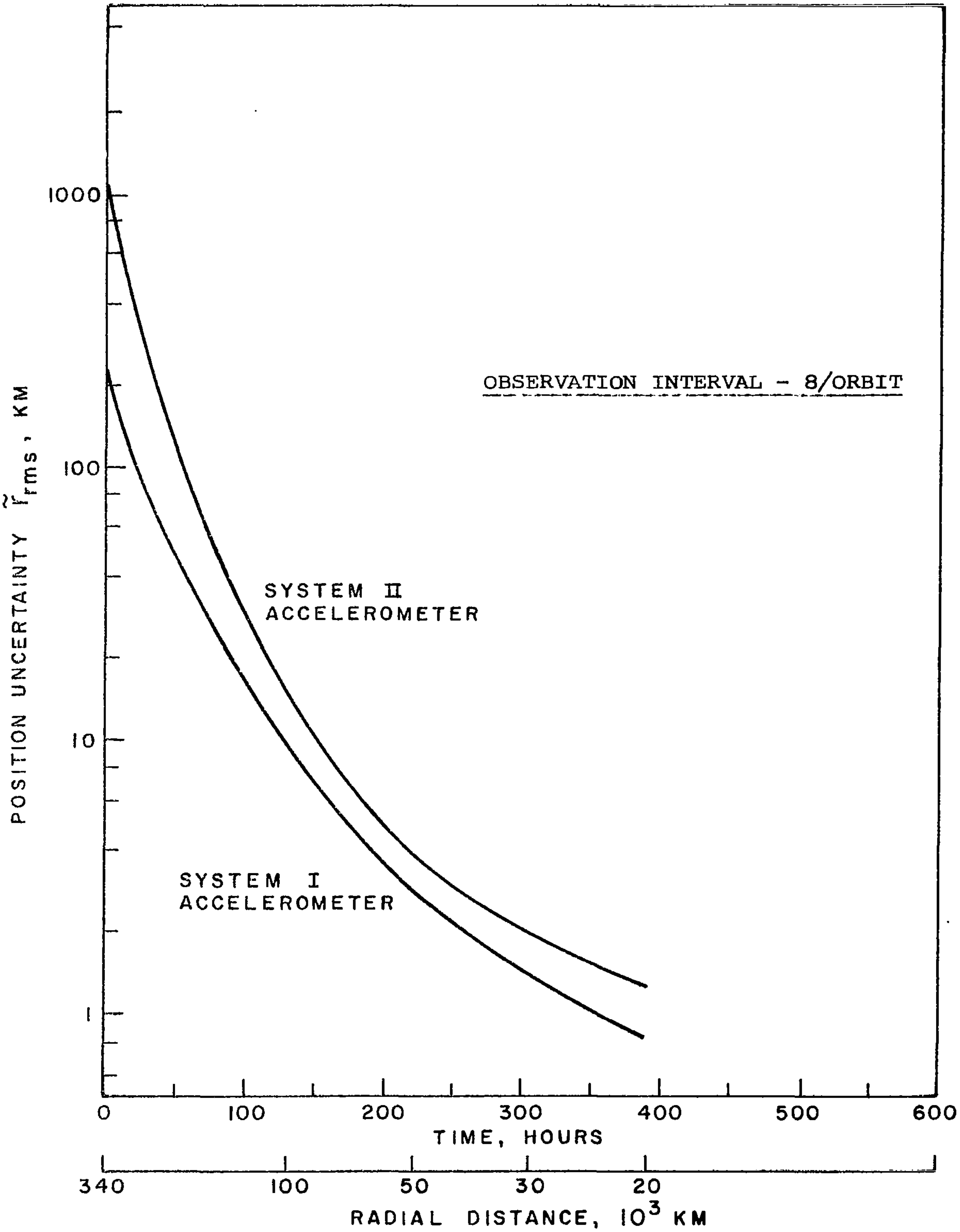

FIGURE 13 POSITION UNCERTAINTY DURING VENUS CAPTURE PHASE, VENUS ORBITER MISSION

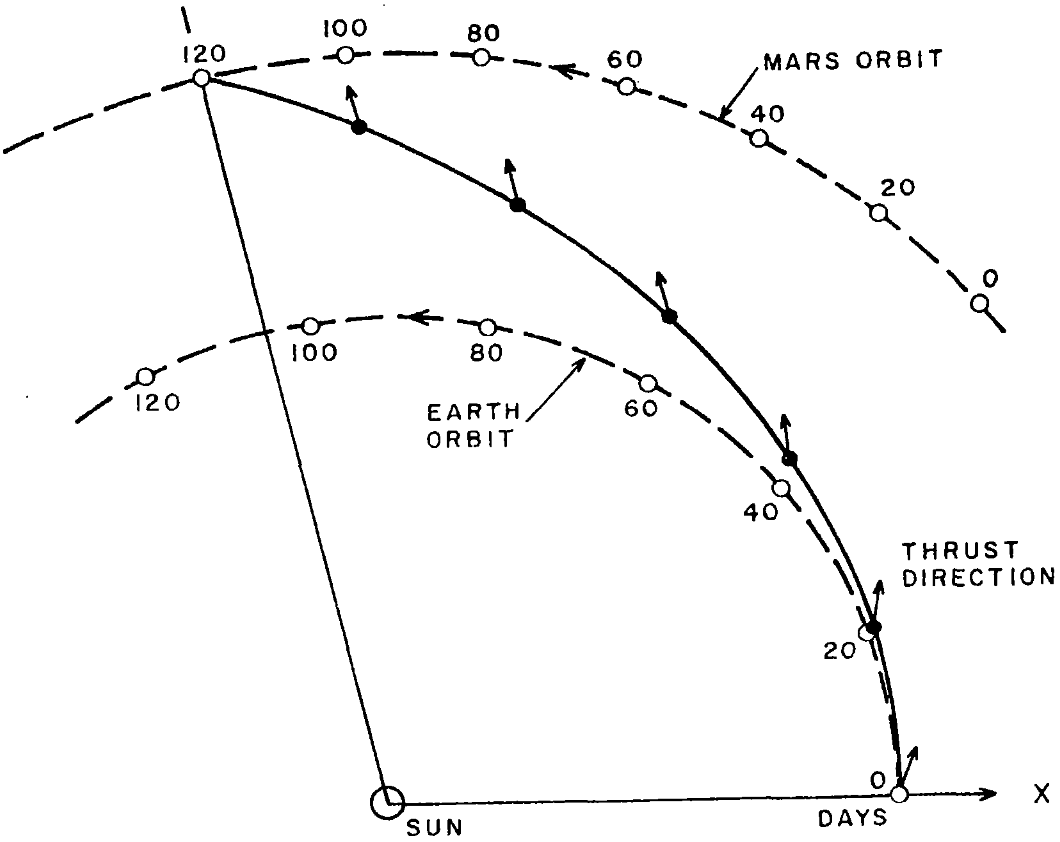

FIGURE 14 MARS FLYBY 120 DAYS, VARIABLE THRUST MODE

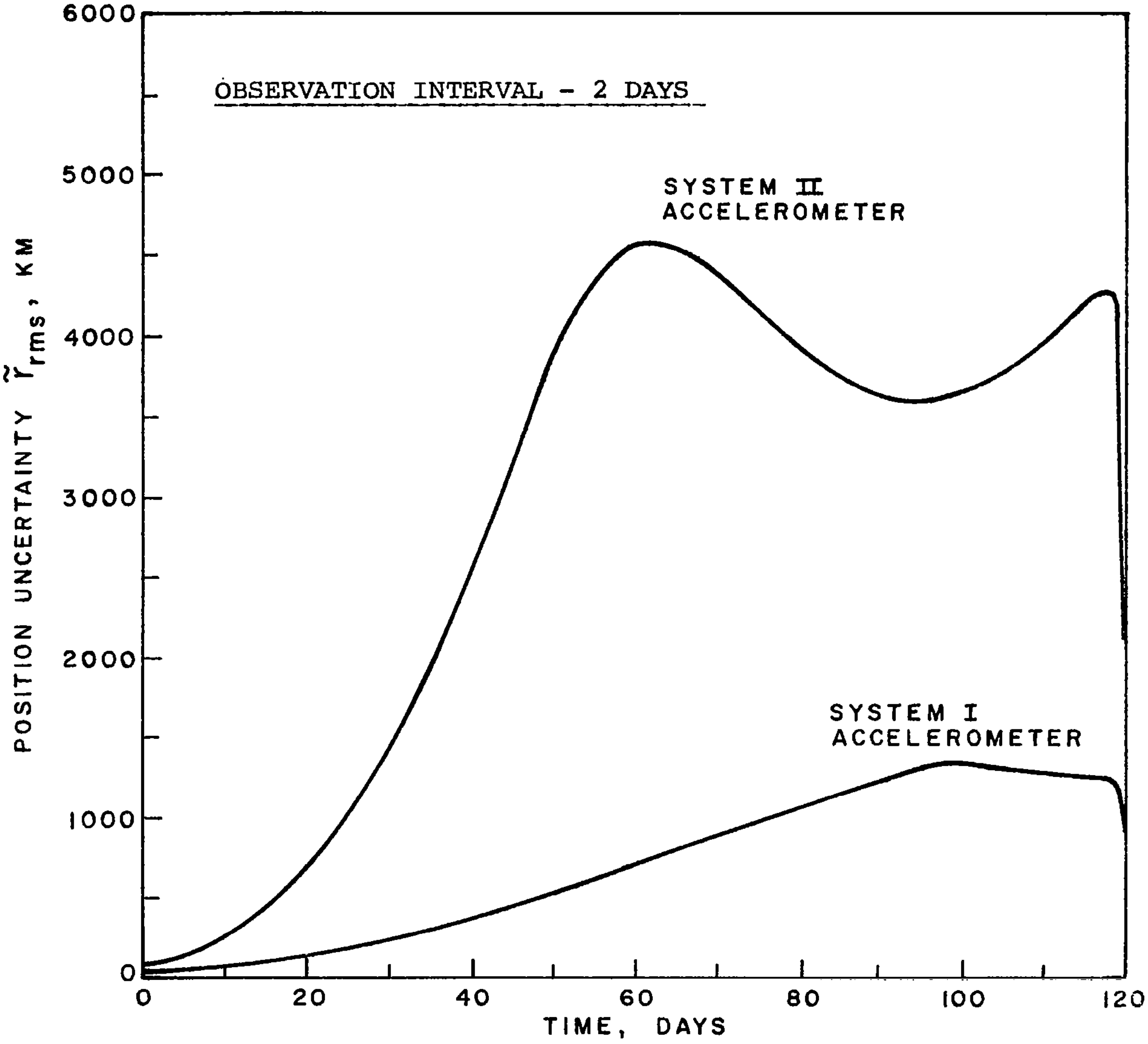

FIGURE 15 POSITION UNCERTAINTY DURING HELIOCENTRIC PHASE, MARS FLYBY MISSION

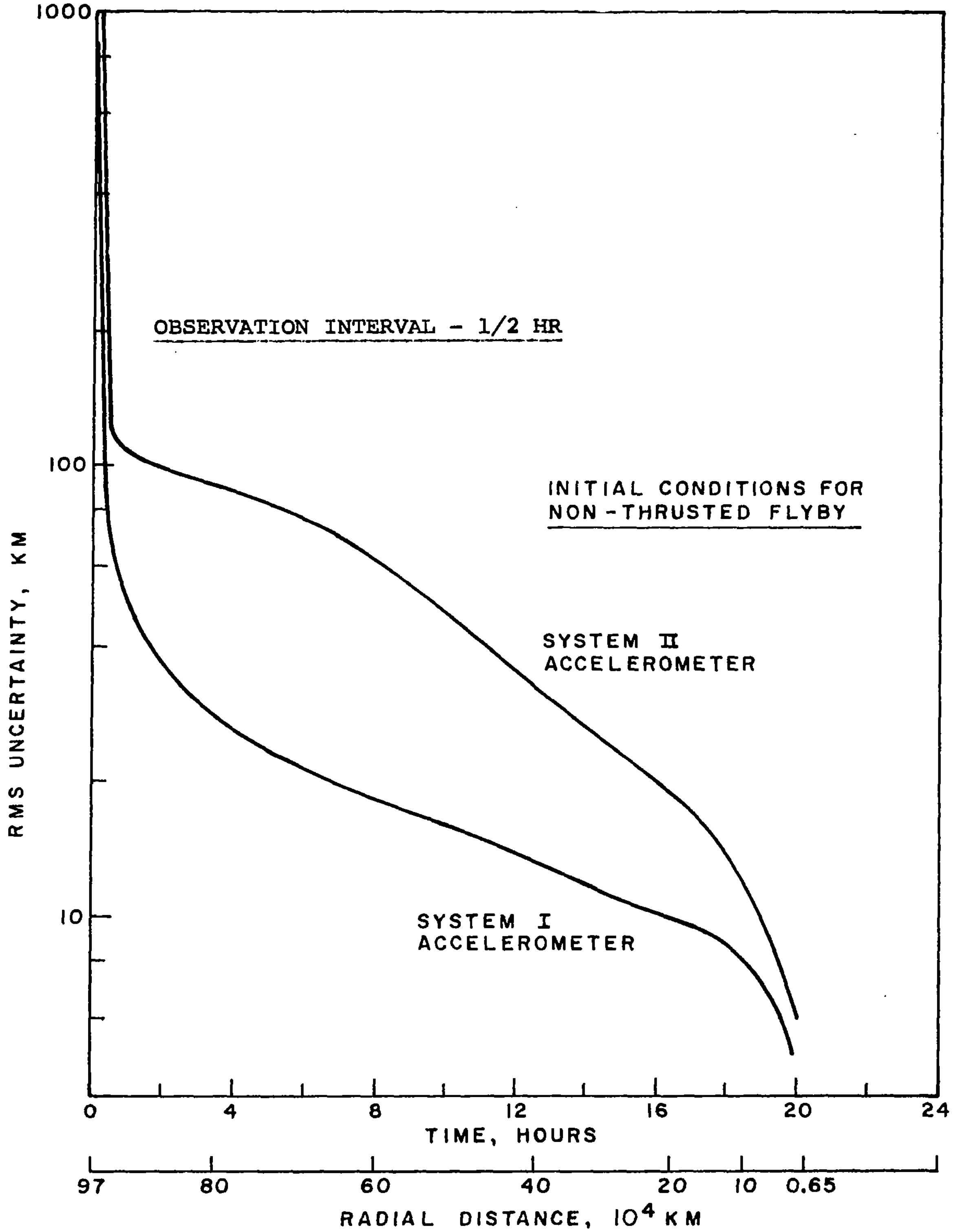

FIGURE 16 UNCERTAINTY IN CLOSEST APPROACH DISTANCE TO MARS, PLANETOCENTRIC PHASE, MARS FLYBY MISSION

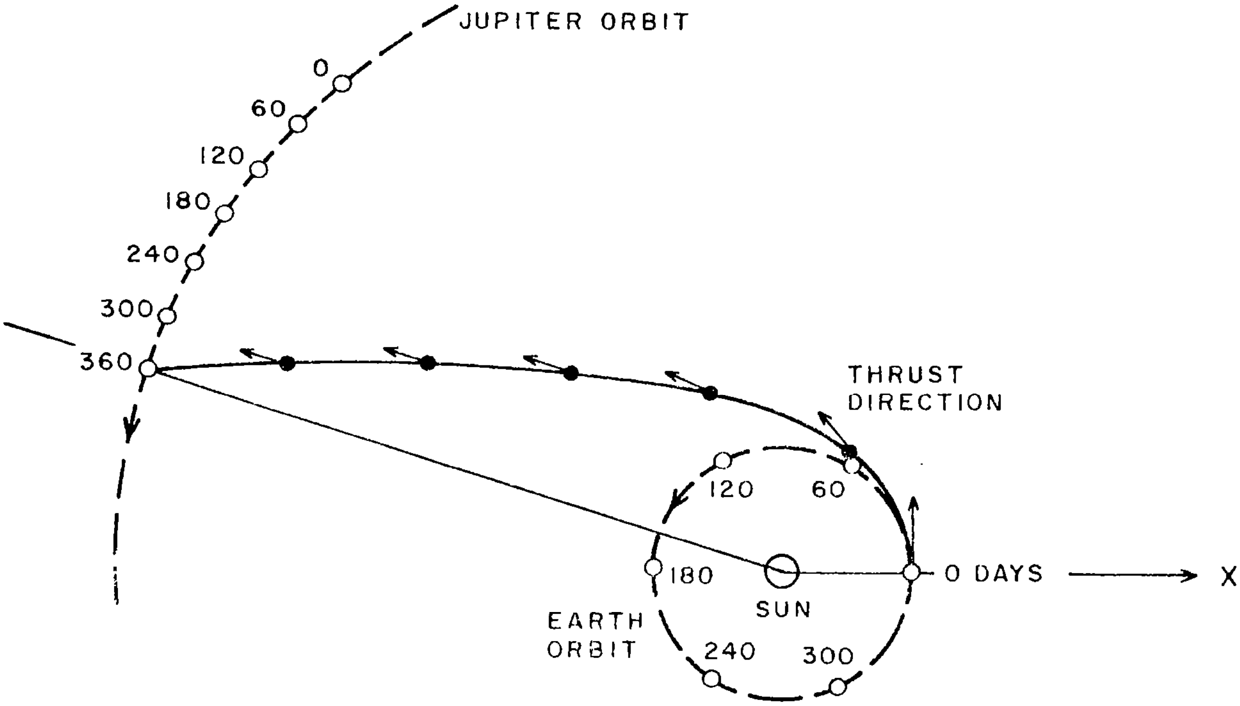

FIGURE 17 JUPITER FLYBY 360 DAYS VARIABLE THRUST MODE

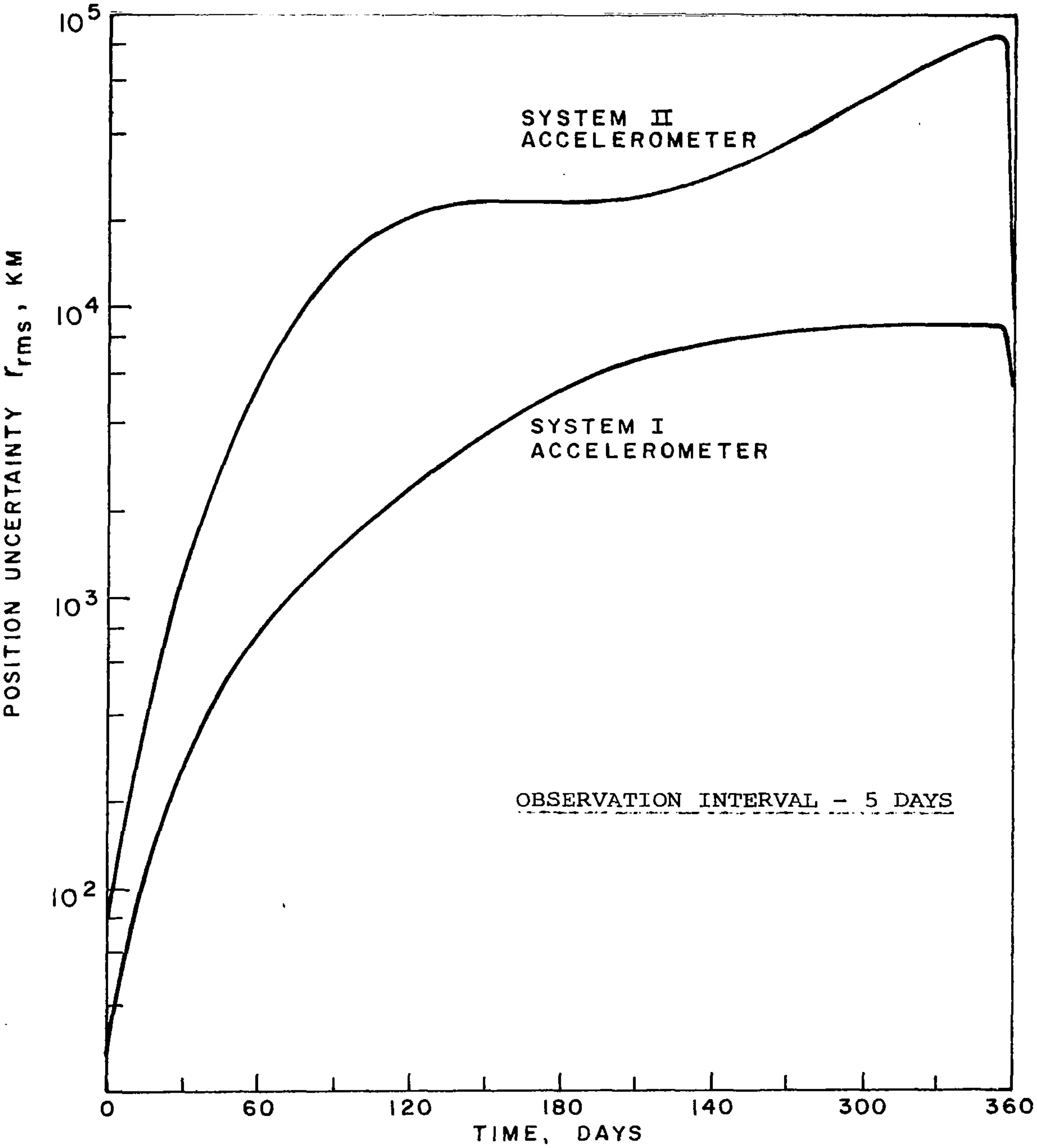

FIGURE 18 POSITION UNCERTAINTY DURING HELIOCENTRIC PHASE, JUPITER FLYBY MISSION

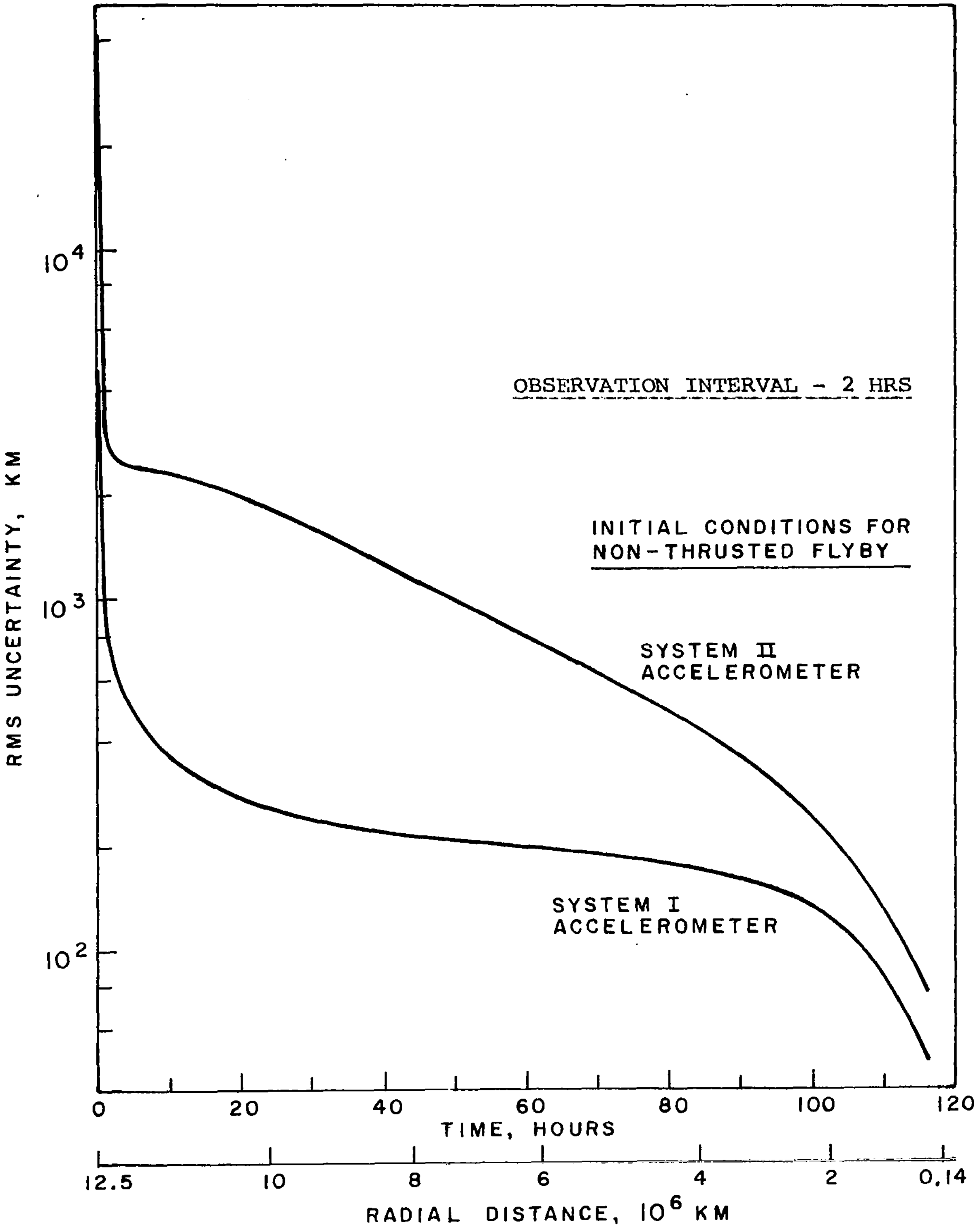

FIGURE 19 UNCERTAINTY IN CLOSEST APPROACH DISTANCE TO JUPITER, PLANETOCENTRIC PHASE, JUPITER FLYBY MISSION

NASA-Langley, 1967 —— 21 CR-740